The Astrophysical Journal Letters, 1006:L63 (17pp), 2026 August 1 https://doi.org/10.3847/2041-8213/ae8af1

Stellar Multiplicity of M Dwarfs with Short-period Giant Planets, and the Characterization of TOI-5628Ab

Tianjun Gan[1,2,3], Alexandrine L'Heureux[4], Charles Cadieux[4,5], Shude Mao[1], Enric Pallé[2,3], Sharon X. Wang[6], Keivan G. Stassun[7,8], Steve B. Howell[9], Benjamin V. Rackham[10,11], Steffani M. Grondin[12], Khalid Barkaoui[2,10,13], Luc Arnold[14], Étienne Artigau[4,15], Artem Burdanov[10], Adam J. Burgasser[16], Douglas A. Caldwell[9,17], David R. Ciardi[18], Karen A. Collins[19], Neil J. Cook[4], René Doyon[4,15], Georgina Dransfield[20,21], Akihiko Fukui[2,22], Michaël Gillon[13], Emmanuel Jehin[23], Felipe Murgas[2,3], Norio Narita[2,22,24], Federico R. Noguer[25], Howard M. Relles[19], Avi Shporer[26], Molly N. Simon[25], Abderahmane Soubkiou[13], Christopher A. Theissen[16], Mathilde Timmermans[13,27], Amaury H. M. J. Triaud[27], Robert T. Zellem[28], S. Zúñiga-Fernández[23], Celso P. Machado[29], Ian R. Mason[29], Michele T. Mazzucato[29], and Jingyuan Zhao[29]

[1] Department of Astronomy, Westlake University, Hangzhou 310030, Zhejiang Province, People's Republic of China; tianjungan@gmail.com
[2] Instituto de Astrofísica de Canarias (IAC), E-38205 La Laguna, Tenerife, Spain
[3] Departamento de Astrofísica, Universidad de La Laguna (ULL), E-38206 La Laguna, Tenerife, Spain
[4] Institut Trottier de Recherche sur les Exoplanètes, Département de Physique, Université de Montréal, Montréal, QC H3C 3J7, Canada
[5] Observatoire de Genève, Département d'Astronomie, Université de Genève, Chemin Pegasi 51, 1290 Versoix, Switzerland
[6] Department of Astronomy, Tsinghua University, Beijing 100084, People's Republic of China
[7] Department of Physics and Astronomy, Vanderbilt University, 6301 Stevenson Center Lane, Nashville, TN 37235, USA
[8] Department of Physics, Fisk University, 1000 17th Avenue North, Nashville, TN 37208, USA
[9] NASA Ames Research Center, Moffett Field, CA 94035, USA
[10] Department of Earth, Atmospheric and Planetary Science, Massachusetts Institute of Technology, 77 Massachusetts Avenue, Cambridge, MA 02139, USA
[11] Kavli Institute for Astrophysics and Space Research, Massachusetts Institute of Technology, 77 Massachusetts Avenue, Cambridge, MA 02139, USA
[12] Department of Astronomy & Astrophysics, University of California San Diego, La Jolla, CA 92093, USA
[13] Astrobiology Research Unit, Université de Liège, 19C Allée du 6 Août, 4000 Liège, Belgium
[14] Canada France Hawaii Telescope (CFHT) Corporation, UAR2208 CNRS-INSU, 65-1238 Mamalahoa Hwy, Kamuela 96743 HI, USA
[15] Observatoire du Mont-Mégantic, Université de Montréal, Montréal, QC H3C 3J7, Canada
[16] Center for Astrophysics and Space Sciences, University of California, San Diego, 9500 Gilman Dr, La Jolla, CA 92093, USA
[17] SETI Institute, Mountain View, CA 94043, USA
[18] NASA Exoplanet Science Institute, Caltech/IPAC, Mail Code 100-22, 1200 E. California Boulevard, Pasadena, CA 91125, USA
[19] Center for Astrophysics |Harvard & Smithsonian, 60 Garden Street, Cambridge, MA 02138, USA
[20] Department of Astrophysics, University of Oxford, Denys Wilkinson Building, Keble Road, Oxford OX1 3RH, UK
[21] Magdalen College, University of Oxford, Oxford OX1 4AU, UK
[22] Komaba Institute for Science, The University of Tokyo, 3-8-1 Komaba, Meguro, Tokyo 153-8902, Japan
[23] Space Sciences, Technologies and Astrophysics Research (STAR) Institute, Université de Liège, 19C Allée du 6 Août, 4000 Liège, Belgium
[24] Astrobiology Center, 2-21-1 Osawa, Mitaka, Tokyo 181-8588, Japan
[25] School of Earth and Space Exploration, Arizona State University, 781 E. Terrace Mall, Tempe, AZ 85287-6004, USA
[26] Department of Physics and Kavli Institute for Astrophysics and Space Research, Massachusetts Institute of Technology, Cambridge, MA 02139, USA
[27] School of Physics & Astronomy, University of Birmingham, Edgbaston, Birmingham B15 2TT, UK
[28] NASA Goddard Space Flight Center, 8800 Greenbelt Road, Greenbelt, MD 20771, USA
[29] Citizen Scientist, Zooniverse c/o University of Oxford, Keble Road, Oxford OX1 3RH, UK
Received 2026 June 1; revised 2026 July 9; accepted 2026 July 11; published 2026 July 29

Abstract

Binary stars are ubiquitous; yet it remains unclear how wide-orbit stellar companions influence the formation of hot Jupiters, particularly around M dwarfs. Here, we first report the discovery of TOI-5628Ab, a giant planet transiting a midtype M dwarf ($M_* = 0.36 \pm 0.02\,M_\odot$) every 4.34 days, accompanied by an associated white dwarf TOI-5628B ($M_{\rm WD} = 0.59 \pm 0.16\,M_\odot$) at a projected distance of about 2500 au. Using TESS, ground-based photometry, and SPIRou radial velocities, we constrain the planet radius to $0.74 \pm 0.04\,R_{\rm J}$ and mass to $0.09 \pm 0.04\,M_{\rm J}$, with a 3σ upper limit of $0.22\,M_{\rm J}$. Building on this system, we further conduct a homogeneous systematic search for comoving stellar companions with projected semimajor axes between 100 and 10,000 au around all M dwarfs with confirmed giant planets with periods smaller than 10 days and radii larger than $0.7\,R_{\rm J}$, as well as a group of field M stars with stellar properties similar to the planet sample, based on the stellar kinematics from Gaia DR3. We measure a stellar multiplicity of $34.2\% \pm 9.5\%$ for M dwarfs hosting short-period giant planets, which is substantially higher than the fraction of $5.3\% \pm 3.7\%$ for the field M stars by approximately a factor of 6. Our results suggest that wide-orbit stellar companions tend to promote the formation of short-period gas giants around M stars with masses $0.21 \leqslant M_* \leqslant 0.64\,M_\odot$, and high-eccentricity migration may play an important role in producing such systems.

Unified Astronomy Thesaurus concepts: M dwarf stars (982); Hot Jupiters (753); Multiple stars (1081); Binary stars (154); Transits (1711); Radial velocity (1332); Astrostatistics (1882)

1. Introduction

Stars are not alone; nearly half of local Sun-like stars were born in pairs or multiples (D. Raghavan et al. 2010; S. S. R. Offner et al. 2023), while low-mass M stars have a multiplicity, defined as the fraction of multiple-star systems in a sample, of about 20% (K. Ward-Duong et al. 2015; J. G. Winters et al. 2019; S. S. R. Offner et al. 2023; C. A. Clark et al. 2024). Whether and how wide-orbit stellar companions influence the formation and evolution of planetary systems, particularly hot Jupiters with orbital period $P \leqslant 10$ days, remains an open question.

High-eccentricity migration is one of the leading channels proposed to explain the existence of short-period hot Jupiter systems (R. I. Dawson & J. A. Johnson 2018). Under this framework, the orbit of a giant planet is excited through mechanisms like scattering (F. A. Rasio & E. B. Ford 1996; S. Chatterjee et al. 2008; E. B. Ford & F. A. Rasio 2008), secular interactions (Y. Wu & Y. Lithwick 2011; C. Petrovich 2015), and Kozai–Lidov mechanism (Y. Kozai 1962; M. L. Lidov 1962; S. Naoz 2016) driven by regular perturbation from an outer massive body such as a stellar companion. Subsequently, the orbit shrinks and circularizes through tidal dissipation (P. Hut 1981; P. P. Eggleton et al. 1998; B. Jackson et al. 2008).

Based on imaging surveys, H. Ngo et al. (2016) found that the multiplicity of Sun-like stars hosting hot Jupiters is 47% ± 4% at projected separations between 50 and 2000 au, approximately 2.9 times higher than the fraction of field stars within the same projected semimajor axis range (see also H. Ngo et al. 2015). A similar finding was reported by C. Fontanive et al. (2019), where the authors searched for wide binary companions among a mixed sample of giant planets and brown dwarfs, and determined a binary fraction of about 79% between 20 and 10,000 au, roughly twice as high as that of field stars. In contrast, later work from M. Moe & K. M. Kratter (2021) proposed that wide-orbit stellar companions have either a negligible or negative effect on the formation of close-in giant planets orbiting G dwarfs by comparing the occurrence rates from transit and radial velocity (RV) surveys.

However, equivalent statistical studies on hot Jupiters around M dwarfs, which provide sensitive tests of planet formation given their high mass ratios among planetary systems (G. Laughlin et al. 2004; S. Ida & D. N. C. Lin 2005; G. M. Kennedy & S. J. Kenyon 2008; B. Liu & J. Ji 2020; R. Burn et al. 2021), are still lacking. This is primarily due to the low occurrence rate of hot Jupiters around M stars compared to their Sun-like counterparts (E. M. Bryant et al. 2023; T. Gan et al. 2023b; R. I. Glusman et al. 2026). Nevertheless, the situation has now changed; the Transiting Exoplanet Survey Satellite (TESS; G. R. Ricker et al. 2015) has yielded around 40 detections of such systems over the last eight years (e.g., T. Gan et al. 2022, 2023a; A. Jordán et al. 2022; J. D. Hartman et al. 2024; S. Kanodia et al. 2024; G. Dransfield et al. 2026; Y. G. C. Frensch et al. 2026), making it possible to look into their demographics.

Here, we first report the discovery and characterization of TOI-5628Ab, a short-period gas giant around a midtype (M3.0 ±1.0) M dwarf with a wide-orbit white dwarf (WD) companion. We next conduct a systematic search for comoving stellar companions around all M dwarfs with confirmed short-period giant planets, determine their multiplicity rate between 100 and 10,000 au, and compare the result with that of field M stars. The Letter is organized as follows. We describe the TESS and SPIRou RV observations in Section 2, perform stellar characterization and a joint analysis in Section 3, carry out the population-level multiplicity study in Section 4, before we conclude in Section 5.

2. TESS Photometry and SPIRou RVs

TOI-5628A (LP 435-59) was monitored by TESS in Sector 49 during the Extended Mission under the two-minute cadence mode (G. R. Ricker et al. 2015). The observations spanned about 1 month, from UT 2022 March 1 to UT 2022 March 25, comprising 13,404 exposures in total. The images were reduced by the Science Processing Operations Center (SPOC; J. C. Smith et al. 2012; M. C. Stumpe et al. 2012, 2014; J. M. Jenkins et al. 2016). We made use of the simple aperture photometry (SAP) produced by SPOC without light dilution correction. After masking out the in-transit signals, we utilized the `celerite` algorithm (D. Foreman-Mackey et al. 2017) to fit a Gaussian process (GP) model with a Matérn-3/2 kernel to the out-of-transit data to detrend the light curve. Figure 1 shows the POSS-II survey image of TOI-5628 taken in 1990 (B. M. Lasker et al. 1996) alongside the TESS target pixel file (TPF) overlaid with the aperture used to extract the photometry, plotted using `tpfplotter` (A. Aller et al. 2020). The gravitationally bound WD TOI-5628B (LP 435-58) located about 23″ (~2500 au, $\Delta T = 2.74$ mag) away from the target star appears in both images, which slightly contaminates the photometric aperture. The dilution effect is modeled and taken into account during the joint fit. The raw, detrended, and phase-folded TESS light curves are shown in the right panel of Figure 1. All light curves from ground-based follow-up observations are presented in Figure A1. The transiting object was also identified as a planet candidate by Planet Hunters TESS citizen scientists program (N. L. Eisner et al. 2021), and registered as a Community TESS Object of Interest (cTOI).

We collected 40 spectra[30] of TOI-5628A between UT 2023 December 24 and UT 2024 December 21 using SPIRou (SpectroPolarimètre InfraROUge; J. F. Donati et al. 2020), a near-infrared (NIR) spectropolarimeter installed on the 3.6 m Canada–France–Hawaii Telescope (CFHT) with a spectral resolution of $R \approx 75{,}000$ and a wavelength range 0.95–2.35 μm. Each spectrum was obtained from a 30 minute exposure with TOI-5628A in fibers A and B without using a simultaneous calibration lamp in fiber C to avoid contamination of the relatively faint science spectra by the bright Fabry–Pérot étalon. The observing set-up results in a median signal-to-noise ratio (SNR) of 23 at order 35 (~1.75 μm) for each spectrum. We reduced the data with the standard reduction pipeline `APERO` v0.7.296 (N. J. Cook et al. 2022). To derive the RVs, we employed the line-by-line (LBL; v0.67.007) framework of É. Artigau et al. (2022). Since TOI-5628A is faint, we chose a high-SNR star of similar spectral type to build a robust template against which the per-line RV can be computed for TOI-5628A. We find GJ 15B (M3.5V; S. Lépine et al. 2013), for which 767 spectra were obtained between UT 2018 December 19 and UT 2022 January 26,[31] provides the best match. After excluding seven spectra with poor data quality, the remaining 760 spectra were used to construct the template. The resulting RVs, with a median precision of 17.6 m s^{-1}, are shown in Figure 2, and the data can be downloaded from ExoFOP.[32] Additional follow-ups,

[30] From programs led by T. Gan (24AS04, 24AD04 and 24AD09) and X. Hua (24BS05).
[31] Telluric-corrected spectra are publicly available through the Canadian Astronomical Data Centre (CADC): https://www.cadc-ccda.hia-iha.nrc-cnrc.gc.ca.
[32] https://exofop.ipac.caltech.edu/tess/target.php?id=135100529

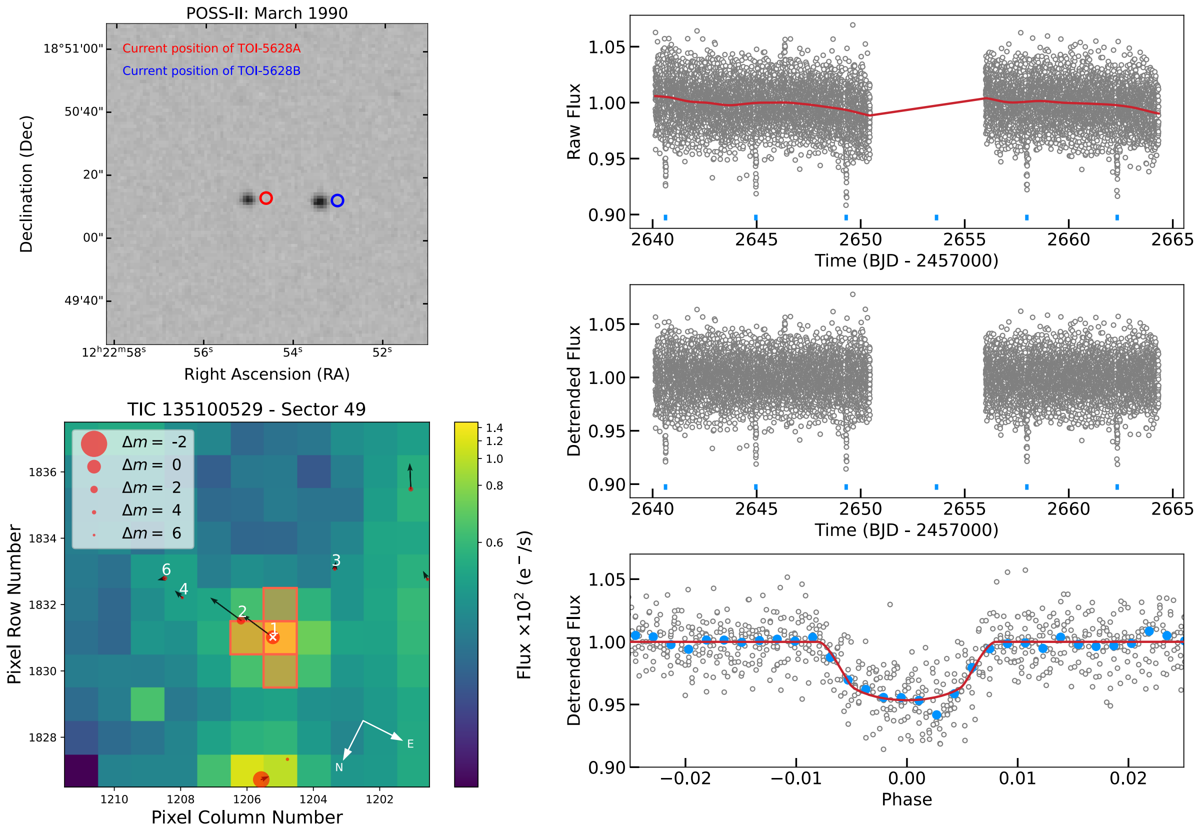

Figure 1. Top left panel: POSS-II image of TOI-5628A and TOI-5628B obtained in 1990. The red and blue circles are the current positions of the two stars. Bottom left panel: TPF plot of TOI-5628A in Sector 49 with the photometric aperture overlaid as the orange shaded region. TOI-5628A is marked as a white cross. The black arrows represent the proper motions of every star. Right panel: raw (top), detrended (middle), and phase-folded (bottom) TESS light curve. The transits are highlighted with blue ticks. The blue dots are the light curve binned to 10 minutes. The red curve is the best-fit model from the joint analysis.

including ground-based photometric, spectroscopic, and imaging observations, are described in Appendix A.

3. Analysis

3.1. Stellar Characterization

3.1.1. Properties of the Host Star TOI-5628A

We assigned an NIR spectral type using the SpeX Prism Library Analysis Toolkit (SPLAT; A. J. Burgasser & Splat Development Team 2017) by comparing the reduced spectrum of TOI-5628A to single-star spectral standards in the IRTF Spectral Library (M. C. Cushing et al. 2005; J. T. Rayner et al. 2009). The best-matching template is the M3V standard AD Leo, with the M3.5V standard GJ 273 providing only a marginally worse match. We therefore adopt an NIR spectral type of M3.0±1.0 for TOI-5628A. Applying the A. W. Mann et al. (2013) relation to this spectrum, we measured an iron abundance of $[\mathrm{Fe/H}] = -0.10 \pm 0.14$ dex.

According to the K-band apparent magnitude from the Two Micron All Sky Survey (2MASS) and stellar parallax from Gaia DR3, we compute the absolute magnitude M_K of TOI-5628A to be 6.695 ± 0.023. We thus obtain the stellar radius $R_* = 0.348 \pm 0.020\,R_\odot$ through the R_*–M_K empirical relation derived by A. W. Mann et al. (2015), which is in agreement with the result $0.350 \pm 0.016\,R_\odot$ derived based on an independent relation between stellar angular diameter and color $V - K_s$ presented in T. S. Boyajian et al. (2014). In addition, we also estimate the stellar mass from the empirical M_K relations[33] of A. W. Mann et al. (2019), leading to $M_\star = 0.356 \pm 0.018\,M_\odot$. This is consistent with the value $0.363 \pm 0.015\,M_\odot$ we obtained using the polynomial relation reported by G. F. Benedict et al. (2016).

Finally, we estimate the stellar effective temperature T_{eff} in three ways. First, we measure the bolometric magnitude of $M_{\mathrm{bol}} = 9.424 \pm 0.094$ mag, which corresponds to a bolometric luminosity of $L_* = 0.013 \pm 0.001\,L_\odot$, after accounting for the bolometric correction $BC_K = 2.729 \pm 0.091$ calculated based on a relation with $V - J$ (A. W. Mann et al. 2015). We then obtain a $T_{\mathrm{eff}} = 3324 \pm 53$ K through the Stefan–Boltzmann law. Similar results, 3259 ± 106 K and 3320 ± 83 K, are also derived when using the temperature–color relations reported in M. J. Pecaut & E. E. Mamajek (2013) and A. W. Mann et al. (2015), respectively.

As an independent determination of the basic stellar parameters, we perform an analysis of the broadband spectral energy distribution (SED) of the star together with the Gaia DR3 parallax (with no systematic offset applied; see, e.g., K. G. Stassun & G. Torres 2021), in order to determine an empirical measurement of the stellar radius, following the procedures described in K. G. Stassun & G. Torres (2016), K. G. Stassun et al. (2017), and K. G. Stassun & G. Torres (2018). Where available, we pull the JHK_S magnitudes from 2MASS, the W1 – W3 magnitudes from the Wide-field Infrared Survey Explorer (WISE), the G, G_{BP}, G_{RP} magnitudes from Gaia, the *ugrizy* magnitudes from Pan-STARRS, and the far-ultraviolet and near-ultraviolet magnitudes from the Galaxy Evolution Explorer (GALEX). Together, the available photometry spans the full stellar SED over the wavelength range of 0.4–10 μm (Figure B1, top left).

[33] https://github.com/awmann/M_-M_K-

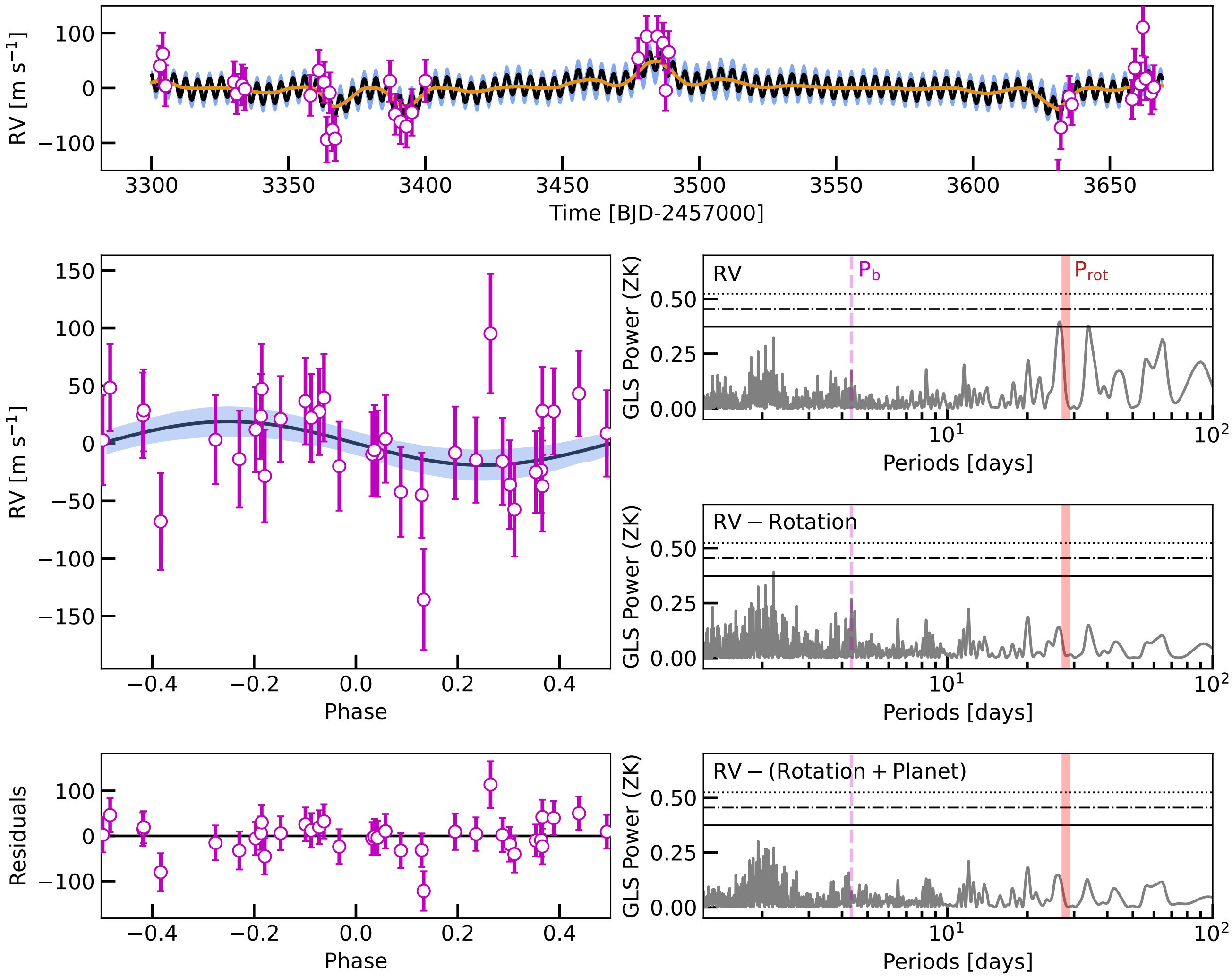

Figure 2. Top panel: time series of SPIRou RVs of TOI-5628A along with the best-fit GP+Keplerian model. The orange curve represents the GP model. Middle left panel: phase-folded RVs after subtracting the best-fit GP model, along with the Keplerian model shown as a black curve. In both panels, the blue shaded region marks the uncertainty at the 68% credibility interval. Bottom left panel: residuals of the fit, in m s^{-1}. The presented RV error bars are the quadratic sum of the measurement uncertainties and the instrument jitter. Right panels: GLS periodograms of the RVs (top), RVs after excluding the GP model (middle), and the residuals after subtracting the GP and Keplerian models (bottom). The orbital period of the planet and the stellar rotation period identified by the ZTF light curve are marked as vertical magenta and red lines. The FAP levels of 10%, 1%, and 0.1% are shown as horizontal solid, dotted–dashed, and dotted lines.

For TOI-5628A, we perform a fit using PHOENIX (T. O. Husser et al. 2013) stellar atmosphere models, with the free parameters being the effective temperature ($T_{\rm eff}$) and metallicity ([Fe/H]), as well as the extinction A_V, which we limit to the maximum line-of-sight value from the Galactic dust maps of D. J. Schlegel et al. (1998). The resulting fit (Figure B1) has a best-fit $A_V = 0.04 \pm 0.04$, $T_{\rm eff} = 3300 \pm 75$ K, [Fe/H] $= 0.0 \pm 0.3$ dex, with a reduced χ^2 of 1.4. Integrating the (unreddened) model SED gives the bolometric flux at Earth, $F_{\rm bol} = 3.61 \pm 0.13 \times 10^{-11}$ erg s^{-1} cm^{-2}. Taking the $F_{\rm bol}$ and $T_{\rm eff}$ together with the Gaia parallax gives the stellar radius, $R_\star = 0.359 \pm 0.016\ R_\odot$, which agrees with the results from the empirical relation estimations within about 1σ. We take the weighted values from different methods and summarize the stellar parameters we adopted in Table 1.

Moreover, we perform a frequency analysis on the long-term light curve from the Zwicky Transient Facility (ZTF; E. C. Bellm et al. 2019; F. J. Masci et al. 2019). We apply the generalized Lomb–Scargle (GLS) periodogram (M. Zechmeister & M. Kürster 2009) to search for periodic modulations. Due to the faintness of the host star, we use the *zr*-band data with 597 measurements after excluding the bad points. Figure C1 shows the periodogram, where a peak is located at 27.9 ± 0.3 days with a false-alarm probability (FAP) below 0.1%. A tentative baseline variation can also be seen in the TESS light curve (Figure 1).

3.1.2. Properties of the Wide-orbit WD TOI-5628B

We similarly fit the SED of the associated WD companion TOI-5628B, using the WD atmosphere models of D. Koester (2010), and enforcing the same A_V as for TOI-5628A (assuming it is at the same distance and line of sight). In that case, we obtain $T_{\rm eff} = 13600 \pm 500$ K, $\log g = 8.0 \pm 0.2$, and $R_{\rm WD} = 0.0117 \pm 0.0012\ R_\odot$. The radius and $\log g$ together imply $M_{\rm WD} = 0.59 \pm 0.16\ M_\odot$. The mass is consistent with the estimation $0.589 \pm 0.021\ M_\odot$ reported in O. Vincent et al. (2024). According to R. Raddi et al. (2022), the cooling age of TOI-5628B is 0.529 ± 0.011 Gyr while the age of the progenitor is uncertain, ranging from 2.5 to 6.9 Gyr, based on the initial-to-final–mass relations from S. Catalán et al. (2008) and J. D. Cummings et al. (2018).

Table 1
Summary of Stellar Parameters for TOI-5628A

Parameter	Value	References
Main Identifiers		
TIC	135100529	TIC V8[a]
Gaia ID	3947322408155619456	Gaia DR3[b]
LP	435-59	Luy63[c]
Equatorial Coordinates		
$\alpha_{J2015.5}$	12:22:54.71	TIC V8
$\delta_{J2015.5}$	+18:50:12.14	TIC V8
Photometric Properties		
TESS (mag)	14.473 ± 0.006	TIC V8
B (mag)	17.987 ± 0.199	APASS[d]
V (mag)	16.902 ± 0.076	APASS
G (mag)	15.571 ± 0.003	Gaia DR3
G_{BP} (mag)	17.045 ± 0.007	Gaia DR3
G_{RP} (mag)	14.386 ± 0.004	Gaia DR3
J (mag)	12.764 ± 0.022	2MASS[e]
H (mag)	12.165 ± 0.024	2MASS
K (mag)	11.907 ± 0.020	2MASS
$W1$ (mag)	11.770 ± 0.022	WISE[f]
$W2$ (mag)	11.612 ± 0.021	WISE
$W3$ (mag)	11.374 ± 0.182	WISE
Astrometric Properties		
ϖ (mas)	9.068 ± 0.044	Gaia DR3
μ_α (mas yr^{-1})	−170.769 ± 0.040	Gaia DR3
μ_δ (mas yr^{-1})	−28.445 ± 0.042	Gaia DR3
Stellar Parameters		
Distance (pc)	110.27 ± 0.54	Gaia DR3
Spectral Type	M3.0 ± 1.0	This work
M_* ($M_\odot$)	0.36 ± 0.02	This work
R_* ($R_\odot$)	0.35 ± 0.02	This work
T_{eff} (K)	3310 ± 100	This work
$[Fe/H]$ (dex)	−0.10 ± 0.14	This work
P_{rot} (days)	27.9 ± 0.3	This work

Notes.
[a] K. G. Stassun et al. (2019).
[b] Gaia Collaboration et al. (2023).
[c] W. J. Luyten (1963).
[d] A. A. Henden et al. (2016).
[e] R. M. Cutri et al. (2003).
[f] E. L. Wright et al. (2010).

While the broadband SED provides a good overall fit to a WD model (Figure B1, top right), spectroscopic confirmation is required to confirm the presence of a WD (and rule out degeneracies with other hot and compact sources, such as subdwarfs). In Section A.2.2, we describe our observations and data reduction of TOI-5628B using Shane/Kast, and present the resulting normalized spectrum in the bottom panel of Figure B1. In principle, a WD's T_{eff} and $\log g$ can be constrained directly through detailed fitting of Balmer line profiles using WD atmosphere models (e.g., D. Koester 2010; P.-E. Tremblay et al. 2011), as these parameters strongly influence the depth and pressure-broadened shape of the lines. However, due to the low SNR of the Shane/Kast spectrum, particularly in the blue region where the lower-order Balmer lines are located, as well as residual flux calibration uncertainties, a reliable quantitative atmospheric fit is not feasible (where the inferred uncertainties on T_{eff} and $\log g$ greatly exceed those obtained via the SED fit). Nevertheless, the spectrum clearly exhibits multiple broad Balmer absorption features at their expected wavelengths, providing robust confirmation of a DA WD. We therefore adopt the T_{eff} and $\log g$ values inferred from the SED fit above for the WD TOI-5628B.

3.2. Joint Analysis of Transits and RVs

We utilize the `juliet` (N. Espinoza et al. 2019) package to perform a joint analysis of all light curves together with the SPIRou RVs, which makes use of `batman` (L. Kreidberg 2015) to construct the light curve model as well as `radvel` (B. J. Fulton et al. 2018) to fit the RVs. The posteriors are determined through dynamic nested sampling using `dynesty` (J. S. Speagle 2020).

According to the frequency analysis of the long-term light curve from the ZTF (E. C. Bellm et al. 2019; F. J. Masci et al. 2019), TOI-5628A has a rotation period of $P_{rot} = 27.9 \pm 0.3$ days (see Section 3.1). Such a periodic modulation also shows up in the GLS periodogram (M. Zechmeister & M. Kürster 2009) of SPIRou RVs (see Figure 2) and is tentatively present in the TESS light curve. We therefore include a GP regression in the modeling with a rotation kernel formulated by D. Foreman-Mackey et al. (2017):

$$k_{i,j}(\tau) = \frac{B}{2+C} e^{-\tau/L}\left[\cos\left(\frac{2\pi\tau}{P_{rot}}\right) + (1+C)\right], \qquad (1)$$

where B is the GP covariance amplitude, C is a balance parameter between the periodic and the nonperiodic terms, $\tau = |t_i - t_j|$ is the time lag between two RV measurements i and j, L is the coherence timescale, and P_{rot} represents the stellar rotational period.

We place wide noninformative priors on most parameters except for the TESS light dilution factor D_{TESS}[34] and P_{rot}, for which we adopt truncated-normal and normal priors (see Table 2). For all ground-based photometry, we set the dilution factors to unity, as the target is well deblended. We adopt a quadratic limb-darkening law for the TESS photometry while a linear law for ground-based data for simplicity (D. M. Kipping 2013). Given the short period of the planet that tidal forces have circularized the orbit ($\tau_{circ} \sim 0.41$ Gyr based on B. Jackson et al. 2008), we opt to fix the orbital eccentricity to zero during the fit. For each instrument, we model an offset and a jitter to characterize additional white noise. We list the priors and the posteriors of key parameters in Table 2. All photometric data along with the best-fit transit models are presented in Figures 1 and A1. Figure 2 displays the RV time series, the phase-folded RVs along with the GLS periodograms of the RVs, the RVs after subtracting the rotation signal, and the RVs after subtracting both the rotation and the planetary signal. The joint analysis reveals that the companion is a giant planet with a period of 4.34 days, a radius ratio of 0.2114 ± 0.0008, and an RV semiamplitude of 21.2 ± 9.1 m s^{-1}, corresponding to a planet radius of $0.74 \pm 0.04\,R_J$ and a mass of $0.09 \pm 0.04\,M_J$ with a 3σ upper limit of $0.22\,M_J$. We then rerun the fit but excluding the GP, and we obtain nearly the same RV semiamplitude but a higher jitter. The GP+Keplerian model is slightly preferred over the Keplerian-only fit with a Bayesian evidence improvement of $\Delta \log Z = 3$. However, we note that telluric correction is particularly challenging for faint targets when the barycentric Earth RV

[34] The dilution factor is defined as $1/(1 + A_D)$, where A_D is the flux ratio between all contaminating stars and the target TOI-5628A.

Table 2
Priors and the Best-fit Values of TOI-5628Ab along with the 68% Credibility Intervals in the Joint Fit

Parameter	Prior	Value	Description
Orbit Parameters			
P (days)	$\mathcal{U}$ (1 , 10)	4.3416612 ± 0.0000015	Orbital period.
T_c (BJD-2457000)	$\mathcal{U}$ (2637 , 2643)	2640.6193 ± 0.0002	Mid-transit time.
r_1	$\mathcal{U}$ (0 , 1)	0.6012 ± 0.0131	Parameterization for p and b[a].
r_2	$\mathcal{U}$ (0 , 1)	0.2114 ± 0.0008	Parameterization for p and b.
e	Fixed	0	Orbital eccentricity.
ω (deg)	Fixed	90	Argument of periapsis.
K (m s^{-1})	$\mathcal{U}$ (0 , 1000)	21.2 ± 9.1	RV semiamplitude.
$\mu_{\rm SPIRou}$ (m s^{-1})	$\mathcal{U}$ (−30000 , −10000)	−20538.5 ± 9.7	RV offset.
$\sigma_{\rm SPIRou}$ (m s^{-1})	$\mathcal{U}$ (0 , 100)	40.5 ± 6.0	RV jitter.
Stellar Parameter			
ρ_* (kg m^{-3})	$\mathcal{LU}$ (10^3 , 10^6)	11507 ± 301	Stellar density of the host star.
Dilution Factors			
$D_{\rm TESS}$	$\mathcal{TN}$ (0.9, 0. 1^2, 0 , 1)	0.879 ± 0.027	…
$D_{\rm Ground}$	Fixed	1	…
GP Hyperparameters			
B	$\mathcal{LU}$ (10^{-6} , 10^6)	$521.22^{+325.76}_{-516.65}$	…
C	$\mathcal{LU}$ (10^{-6} , 10^6)	$1.32^{+61.86}_{-1.30}$	…
L	$\mathcal{LU}$ (10^{-2} , 10^2)	$11.91^{+24.81}_{-11.43}$	…
$P_{\rm rot}$	$\mathcal{N}$ (27.9 , 2. 0^2)	27.36 ± 1.56	…
Derived Parameters			
R_p/R_*	…	0.2114 ± 0.0008	Scaled planet radius.
a/R_*	…	22.5498 ± 0.1949	Scaled semimajor axis.
b	…	0.4018 ± 0.0196	Impact parameter.
i (deg)	…	88.98 ± 0.06	Orbital inclination.
Physical Parameters			
R_p ($R_{\rm J}$)	…	0.74 ± 0.04	Planet radius.
M_p ($M_{\rm J}$)	…	0.09 ± 0.04	Planet mass.
$\log g_{\rm p}$ (cgs)	…	2.61 ± 0.27	Planet surface gravity.
a (au)	…	0.0368 ± 0.021	Semimajor axis.
ρ_p (g cm^{-3})	…	0.29 ± 0.14	Planet density.
$T_{\rm eq}$[b] (K)	…	492 ± 15	Equilibrium temperature.

Notes. $\mathcal{N}(\mu\ ,\ \sigma^2)$ is a normal prior with mean μ and standard deviation σ, while $\mathcal{TN}$ (μ, σ^2, a , b) means a truncated-normal prior ranging from a to b. $\mathcal{U}$(a , b) represents a uniform prior between a and b, while $\mathcal{LU}$(a , b) stands for a log-uniform prior between a and b.
[a] The parameters p and b are the companion-to-star radius ratio and the impact parameter (N. Espinoza 2018).
[b] We assume albedo $A_B = 0$.

(BERV) approaches the stellar systemic velocity, causing stellar lines and telluric features from common species (e.g., H_2O and OH) to overlap (e.g., L. Parc et al. 2025; A. Osborn et al. 2026; A. Srivastava et al. 2026). In our dataset, the target remains outside this "BERV-crossing" regime for most observations, with only six exposures in 2024 June (BJD∼2460485) potentially affected. Consequently, we cannot rule out the possibility that part of the variability captured by the GP component arises from residual telluric contamination.

In addition to the joint fit, we also carry out a transit timing variation (TTV) analysis for individual transits. We find no significant TTVs, and all timings agree with the linear ephemeris within 5 minutes.

4. Multiplicity of M Dwarfs with Short-period Giant Planets between 100 and 10,000 au

Putting the TOI-5628Ab system into a broader context, it turns out that wide-orbit stellar companions around M dwarfs harboring short-period giant planets are not rare, and several cases have been reported (A. Jordán et al. 2022; C. I. Cañas et al. 2023; L. M. Bernabò et al. 2024; E. M. Bryant et al. 2024; J. D. Hartman et al. 2024; S. Kanodia et al. 2024; V. Reji et al. 2025; Y. G. C. Frensch et al. 2026). However, the detections of these stellar companions relied on different methods such as high-angular-resolution speckle imaging, adaptive optics observations, and Gaia DR2 or DR3 kinematics (Gaia Collaboration et al. 2018, 2023). Hence, the sample is heterogeneous and not appropriate for demographics. More importantly, it is yet unclear if wide-orbit stellar companions promote or impede the formation of hot Jupiters around low-mass stars. To address this question, we carry out a homogeneous systematic search for comoving stellar companions with projected distance between 100 and 10,000 au around M dwarfs hosting short-period giant planets based on the stellar kinematical information provided in Gaia DR3. We measure the multiplicity of M dwarfs hosting giant planets with orbital periods below 10 days and radii above 0.7 $R_{\rm J}$, and then compare our finding with that of the field M dwarfs. We outline the construction of the planet sample and our search for wide-orbit companions in Section 4.1, and we present the multiplicity result of field M dwarfs within the same projected semimajor range in Section 4.2 before summarizing in Section 4.3.

4.1. Planet Sample Construction and Comoving Companion Search

We retrieve the list of hot Jupiters around M dwarfs from the NASA Exoplanet Archive (R. L. Akeson et al. 2013; J. L. Christiansen et al. 2025) on UT 2026 May 1 using the following selection criteria:

1. Stellar effective temperature $T_{\rm eff} \leqslant 4000$ K;
2. Stellar mass $M_* \leqslant 0.65\,M_\odot$;
3. Orbit period $P \leqslant 10$ days;
4. Planets with radius $R_p \geqslant 0.7\,R_{\rm J}$;
5. Planets with mass determination or upper limits from RV observations.

We define hot Jupiters as planets with orbital periods $P \leqslant 10$ days and radii $R_p \geqslant 0.7\,R_{\rm J}$ throughout this work. After including TOI-5628Ab reported in this work, our planet sample contains a total of 38 systems. The host stars in the resulting sample have effective temperatures $3000 \lesssim T_{\rm eff} \lesssim 4000$ K, stellar masses $0.21 \lesssim M_* \lesssim 0.64\,M_\odot$, stellar distances $70 \lesssim d \lesssim 400$ pc, and TESS-band magnitude $12.5 \lesssim T{\rm mag} \lesssim 15.0$. We record their Gaia DR3 ID, R.A. (α), decl. (δ) and distance.

To evaluate the multiplicity, we follow the methodology proposed in K. El-Badry et al. (2021) to identify comoving companions with analogous proper motions and parallaxes. In particular, we perform a cone search centered at the (α, δ) coordinates of each system with a radius boundary extending to 15,000 au. We conservatively expand the projected radius limit here to account for the uncertainties on stellar position and distance reported in the literature. For every neighboring source, we examine its kinematical properties, and we regard a companion as a comoving star if it satisfies the conditions below:

1. The projected distance between the host and the companion is between 100 and 10,000 au:
$$100\ {\rm au} \leqslant \frac{1000}{\varpi_1\ {\rm mas}^{-1}} \times \rho_{\rm dist} \leqslant 10,000\ {\rm au}, \qquad (2)$$
where ϖ_1 is the parallax of the target star, and $\rho_{\rm dist}$ is the projected separation distance between the target and the companion in units of arcsec, both taken from Gaia DR3.
2. The proper motion difference between the target and the companion is within 5 km s^{-1} with a 2σ tolerance, or equivalently:
$$|\Delta\mu| \leqslant 1.05\ {\rm mas\ yr}^{-1} \times (\varpi_1 + 2\sigma_{\varpi_1})\ {\rm mas}^{-1}, \qquad (3)$$
where $|\Delta\mu| = \sqrt{(\mu_{\alpha_1} - \mu_{\alpha_2})^2 + (\mu_{\delta_1} - \mu_{\delta_2})^2}$, μ_{α_1}, μ_{δ_1}, μ_{α_2}, μ_{δ_2} are the proper motions of the target and companion along the direction of R.A. and decl., ϖ_1 and σ_{ϖ_1} are the parallax of the target star and its uncertainty.
3. The parallaxes of the target and the companion are consistent within 5σ:
$$|\Delta\varpi| \leqslant 5\sqrt{\sigma^2_{\varpi_1} + \sigma^2_{\varpi_2}}, \qquad (4)$$
where $|\Delta\varpi| = |\varpi_1 - \varpi_2|$, σ_{ϖ_1} and σ_{ϖ_2} are the parallax uncertainties of the target and the companion. While K. El-Badry et al. (2021) proposed a 2σ level parallax consistency, we loosen the constraint to 5σ following M. Rice et al. (2022), but we emphasize that the choice here will not change the conclusion.

Among the total sample of 38 systems, our systematic search leads to the detections of 14 comoving stellar companions in 13 systems, including the identification of a stellar companion TIC 46432937B that was not reported in the previous work (J. D. Hartman et al. 2024). Although two comoving companions of TOI-6034 were alerted by the search pipeline, the second object (Gaia DR3 2270399053598645120 at 8661 au) has large uncertainties on its kinematics, and it is likely a background star according to its parallax. However, this ambiguous companion will not affect our statistics as we are investigating the multiplicity. We summarize the target and companion information in Table 3.

Our searching result can be simply converted to a multiplicity of $P({\rm Comp}|{\rm HJ}) = 34.2\% \pm 9.5\%$ for M dwarfs harboring hot Jupiters, where the uncertainty comes from Poisson noise. We note that the multiplicity derived here should be treated as a lower limit, as we do not consider the detection sensitivity of Gaia. For example, the planetary system HATS-74Ab has a bound stellar neighbor denoted as HATS-74B at 238.4 ± 3.9 au found by Keck/NIRC2 AO observations (A. Jordán et al. 2022), but its kinematical information is not recorded in Gaia DR3 due to its faintness and small projected separation distance.

In addition to the radius-based hot Jupiter sample ($R_p \geqslant 0.7\,R_{\rm J}$), we repeat our analysis using a mass-based planet sample. We filter out hot Jupiters with mass above $0.3\,M_{\rm J}$, leading to a total of 31 systems except for TOI-762, TOI-3629, TOI-3757, TOI-3984, TOI-5628, TOI-5634 and TOI-6894 listed in Table 3. Among them, a total of nine systems have comoving stellar companions, yielding a multiplicity of $P({\rm Comp}|{\rm HJ}) = 29\% \pm 10\%$. This is consistent with our previous estimation within 1σ. Therefore, our result is not sensitive to the definition of hot Jupiters.

4.2. Multiplicity of Field M Dwarfs

We adopt two approaches to measure the multiplicity of field M dwarfs within the same projected distance range (100–10,000 au), which deliver consistent results.

Based on the cool dwarf list (cooldwarfs_v8; P. S. Muirhead et al. 2018) embedded in the TESS input Catalog v8.2 (TIC; K. G. Stassun et al. 2019), we filter out field M dwarfs that have similar brightness (Tmag), distance, effective temperature, and mass as our planet sample. We require the field M dwarfs in our sample to have flux contamination below 0.1, ensuring relatively accurate stellar properties. A total of 546,681 field M dwarfs are left. We employ a Monte Carlo method by randomly choosing 38 field stars, the same size as our planet sample, rerunning the companion search pipeline, and computing the multiplicity P(Comp) in the same way introduced in Section 4.1. We repeat the same process 1000 times and record the multiplicity value measured in each trial. Figure 3 shows the multiplicity distribution of field M dwarfs. We take the median and standard deviation of the distribution as the final multiplicity and its corresponding uncertainty, leading to $P({\rm Comp}) = 5.3\% \pm 3.7\%$. Without adding the

Table 3
Kinematical Properties of M dwarfs Hosting Hot Jupiters and their Comoving Companions from the Systematic Search

Target	Target ID[a]	$\mu_{\alpha 1}$ (mas yr^{-1})	$\mu_{\delta 1}$ (mas yr^{-1})	ϖ_1 (mas)	Companion ID	$\mu_{\alpha 2}$ (mas yr^{-1})	$\mu_{\delta 2}$ (mas yr^{-1})	ϖ_2 (mas)	$\rho_{\rm dist}$ (arcsec)	Projected Distance (au)
HATS-6	2966680597368750720	−2.568 ± 0.015	7.371 ± 0.018	5.892 ± 0.019	…	…	…	…	…	…
HATS-71	4710594412266148352	79.128 ± 0.029	−26.985 ± 0.027	7.112 ± 0.024	…	…	…	…	…	…
HATS-74	3545653561942122368	−38.992 ± 0.043	39.578 ± 0.034	3.425 ± 0.042	…	…	…	…	…	…
HATS-75	5082914338199586560	12.716 ± 0.013	−1.687 ± 0.021	5.061 ± 0.021	…	…	…	…	…	…
Kepler-45	2053562475706063744	4.646 ± 0.036	−21.589 ± 0.036	2.598 ± 0.033	…	…	…	…	…	…
NGTS-1	4821739369794767744	−31.887 ± 0.017	−41.077 ± 0.021	4.594 ± 0.017	…	…	…	…	…	…
TIC 46432937	2984391358868786816	−13.365 ± 0.013	36.962 ± 0.012	11.031 ± 0.013	2984391358868786560	−14.133 ± 0.020	37.209 ± 0.018	11.015 ± 0.020	39.709	3599.865
TOI-519	5707485527450614656	−41.959 ± 0.029	29.074 ± 0.027	8.681 ± 0.037	…	…	…	…	…	…
TOI-530	3353218995355814656	13.622 ± 0.027	−62.524 ± 0.023	6.770 ± 0.028	…	…	…	…	…	…
TOI-762	5362352744504000256	−159.174 ± 0.020	−24.780 ± 0.020	10.118 ± 0.023	5362352744496315264	−157.370 ± 0.126	−24.379 ± 0.123	9.792 ± 0.144	3.290	325.151
TOI-2379	6521531466699512064	16.575 ± 0.014	1.750 ± 0.018	4.755 ± 0.018	…	…	…	…	…	…
TOI-2384	4699702272124241152	9.257 ± 0.061	−52.662 ± 0.053	5.322 ± 0.044	4699702272123475328	8.013 ± 0.623	−51.041 ± 0.255	5.052 ± 0.167	0.815	153.055
TOI-3235	6107144260251920000	−170.503 ± 0.028	−64.264 ± 0.023	13.781 ± 0.027	…	…	…	…	…	…
TOI-3288	6685431748042347776	−6.566 ± 0.022	−20.080 ± 0.014	4.969 ± 0.025	6685431748040148992	−6.719 ± 0.114	−20.952 ± 0.073	5.384 ± 0.120	2.131	428.902
TOI-3629	2881820324294985856	185.707 ± 0.012	1.010 ± 0.012	7.667 ± 0.017	…	…	…	…	…	…
TOI-3714	178924390476792320	19.826 ± 0.025	−70.762 ± 0.020	8.839 ± 0.022	178924390476838784	18.805 ± 0.252	−70.672 ± 0.205	8.847 ± 0.227	2.659	300.800
TOI-3757	996878131494639488	−9.032 ± 0.021	−43.128 ± 0.018	5.598 ± 0.021	…	…	…	…	…	…
TOI-3984	1291955578869575552	−48.951 ± 0.016	42.647 ± 0.020	9.184 ± 0.019	1291955574574621056	−50.379 ± 0.163	40.950 ± 0.212	9.057 ± 0.202	3.292	358.448
TOI-4201	2997312063605005056	11.731 ± 0.017	6.053 ± 0.018	5.291 ± 0.019	…	…	…	…	…	…
TOI-4666	4855422771071903232	4.122 ± 0.014	−22.135 ± 0.019	6.488 ± 0.016	…	…	…	…	…	…
TOI-4860	3571038605366263424	−177.238 ± 0.039	−5.430 ± 0.033	12.377 ± 0.034	…	…	…	…	…	…
TOI-5007	5833386583912265728	−13.515 ± 0.026	−29.914 ± 0.025	4.909 ± 0.022	…	…	…	…	…	…
TOI-5205	1842656663520849024	41.678 ± 0.022	52.074 ± 0.024	11.464 ± 0.026	…	…	…	…	…	…
TOI-5292	2610422023759160576	−8.733 ± 0.041	−6.862 ± 0.039	2.790 ± 0.042	2610422028054589824	−9.300 ± 0.171	−7.163 ± 0.169	2.766 ± 0.178	9.400	3369.006
TOI-5293	2640121486388076032	−17.131 ± 0.031	0.487 ± 0.024	6.165 ± 0.028	2640121482094497024	−16.497 ± 0.152	−0.079 ± 0.119	6.274 ± 0.133	3.538	573.956
TOI-5344	52359538285081728	40.325 ± 0.028	−22.194 ± 0.020	7.305 ± 0.023	…	…	…	…	…	…
TOI-5349	58372904816938240	37.203 ± 0.029	−19.559 ± 0.024	5.262 ± 0.026	…	…	…	…	…	…
TOI-5573	1023967108706495360	−3.586 ± 0.034	−56.841 ± 0.034	5.335 ± 0.038	…	…	…	…	…	…
TOI-5628	3947322408155619456	−170.769 ± 0.040	−28.445 ± 0.042	9.068 ± 0.044	3947322403860036352	−170.202 ± 0.094	−28.622 ± 0.088	8.972 ± 0.097	22.674	2500.436
TOI-5634	3979511431397114752	−60.799 ± 0.056	−25.488 ± 0.052	3.090 ± 0.059	3979511431397963008	−60.802 ± 0.213	−25.625 ± 0.207	2.899 ± 0.234	3.815	1234.784
TOI-5688	1363205856494897024	−0.910 ± 0.034	64.930 ± 0.036	4.400 ± 0.029	1363205856494896896	−0.693 ± 0.087	64.965 ± 0.089	4.282 ± 0.073	4.885	1110.252
TOI-5916	1741429438313012608	−8.816 ± 0.039	−25.598 ± 0.040	5.097 ± 0.042	…	…	…	…	…	…
TOI-6034	2270404997834401664	−2.430 ± 0.020	−5.109 ± 0.021	8.512 ± 0.016	2270407952771897472	−2.238 ± 0.016	−5.556 ± 0.017	8.528 ± 0.014	40.068	4707.269
…	…	…	…	…	2270399053598645120	1.470 ± 1.820	2.964 ± 1.796	4.637 ± 1.346	73.725	8661.279
TOI-6303	239050153051494272	33.035 ± 0.021	−35.352 ± 0.018	6.587 ± 0.019	…	…	…	…	…	…
TOI-6330	407530931116600320	−36.516 ± 0.032	−45.080 ± 0.025	6.967 ± 0.027	…	…	…	…	…	…
TOI-6383	473934011733049856	41.023 ± 0.035	−51.299 ± 0.032	5.847 ± 0.031	473934007432818688	41.016 ± 0.167	−51.283 ± 0.155	6.099 ± 0.158	18.151	3104.601
TOI-6894	3917278287286247808	−146.897 ± 0.056	22.227 ± 0.053	13.684 ± 0.053	…	…	…	…	…	…
TOI-7149	1200751810900182400	−7.698 ± 0.039	12.882 ± 0.041	7.860 ± 0.046	…	…	…	…	…	…

Note.
[a] Gaia DR3 ID (Gaia Collaboration et al. 2023).

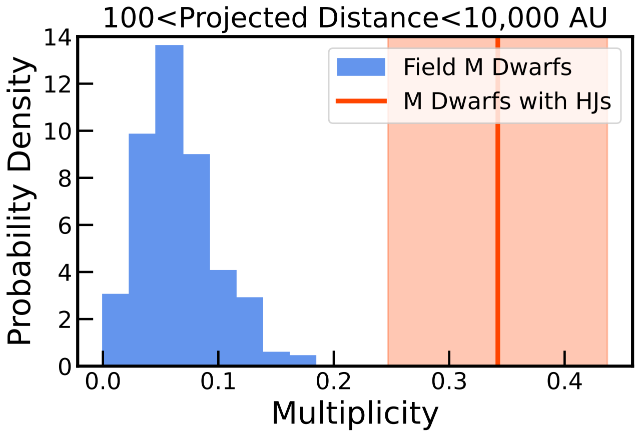

Figure 3. Comparison of the stellar multiplicity of M dwarfs with hot Jupiters and field M stars at projected separations between 100 and 10,000 au. The multiplicity of the planet sample, $P(\mathrm{Comp}|\mathrm{HJ}) = 34.2\% \pm 9.5\%$, is indicated as a vertical red line with the shaded region marking the 1σ uncertainty. The multiplicity of field M dwarfs, $P(\mathrm{Comp}) = 5.3\% \pm 3.7\%$, is shown as a histogram based on the search for 1000 sets of randomly selected field M stars with properties matched to those of the planet sample.

aforementioned flux contamination criterion that potentially excludes high-mass bright comoving companions, we have 824,253 field M dwarfs left. We repeat the same analysis, and we derive a slightly higher multiplicity of $P(\mathrm{Comp}) = 8.6\% \pm 4.5\%$. A similar result here is expected, as the majority of wide-orbit comoving companions around M dwarfs are skewed toward faint late-type M stars with smaller masses, hence having low light contamination ratios (K. Ward-Duong et al. 2015; K. El-Badry et al. 2019; S. S. R. Offner et al. 2023).

In addition, we also explore the multiplicity of field M dwarfs with the help of results from an infrared adaptive optics survey on local M dwarfs within 15 pc (K. Ward-Duong et al. 2015), which derived the companion frequency in six different projected separation bins between 3 and 10,000 au. We retrieve the observational results in Figure 16 of K. Ward-Duong et al. (2015), and fit a standard Gaussian function to approximate the data. We obtain

$$\frac{dP}{d\log a}\Delta\log a = 0.09 \times e^{\frac{(\log a+0.395)^2}{2\times 2.13^2}}, \tag{5}$$

where $\Delta\log a = (4 - \log 3)/6 = 0.587$ is the binning size used in K. Ward-Duong et al. (2015). To constrain the upper limit on the multiplicity of field M dwarfs between 100 and 10,000 au, we integrate Equation (5) between $\log a_{\min} = 2$ and $\log a_{\max} = 4$:

$$P(\mathrm{Comp}) \leqslant \int_{\log a_{\min}}^{\log a_{\max}} \frac{dP}{d\log a}\, d\log a \approx 9.0\%, \tag{6}$$

which agrees with the first-method measurement $P(\mathrm{Comp}) = 5.3\% \pm 3.7\%$ within 1σ. The result 9.0% from the second approach is, in fact, the companion frequency, quantifying the total number of companions within a sample, which is intrinsically equal to or higher than the multiplicity that quantifies the number of multiple-star systems within a sample. Moreover, it has been corrected for incompleteness (see Section 5.6 in K. Ward-Duong et al. 2015). Both reasons explain why it is slightly higher than the first estimate. Consequently, we adopt the first multiplicity value in the following analysis for consistency.

4.3. Multiplicity Comparison between the Planet and Field M Dwarf Sample

Based on $P(\mathrm{Comp}|\mathrm{HJ})$ and $P(\mathrm{Comp})$, one can compute the probability ratio $P(\mathrm{HJ}|\mathrm{Comp})/P(\mathrm{HJ})$ through the Bayes' theorem:

$$\frac{P(\mathrm{HJ}|\mathrm{Comp})}{P(\mathrm{HJ})} = \frac{P(\mathrm{Comp}|\mathrm{HJ})}{P(\mathrm{Comp})} \approx 6.5. \tag{7}$$

Our result indicates that a wide-orbit stellar companion between 100 and 10,000 au enhances the formation efficiency of hot Jupiters around M dwarfs by roughly a factor of 6 compared to isolated single M stars. Relevant works from C. Ziegler et al. (2020), C. A. Clark et al. (2024), and R. A. Matson et al. (2025) all pointed out that the projected separation distribution for M dwarf multiples that are known to host planets peaks beyond 100 au, indicating that close-in (<100 au) stellar companions probably suppress the formation of planets in M dwarf binaries while wide-orbit stellar companions may not inhibit the process.

We caution the readers, however, that our field M dwarf sample does not account for metallicity, as the stellar metallicity is not available in the TIC and it necessitates invoking spectroscopic information. Nonetheless, we emphasize that this effect has a minor impact on our finding, and even probably strengthens our conclusions. T. Gan et al. (2025) found that giant planets, regardless of their orbital periods, favor metal-rich M dwarfs with a median metallicity [Fe/H] of about 0.3 dex (see also G. Dransfield et al. 2026), whereas local field M dwarfs are mostly of solar metallicity. With lower metallicities than those of M stars hosting hot Jupiters, field M stars are, in principle, more likely to reside in a binary configuration (i.e., higher multiplicity rate) according to observations (e.g., M. Moe et al. 2019). This expectation conflicts with the feature we spotted here; a lower multiplicity rate among field M dwarfs compared to those hosting hot Jupiters. However, a few works also argued that the stellar multiplicity rate has invariant or even nonmonotonic dependence on metallicity when moving beyond 250 au (K. El-Badry et al. 2019; H.-C. Hwang et al. 2021; S. S. R. Offner et al. 2023), so we are not able to draw a firm conclusion regarding whether metallicity significantly affects our results. A detailed investigation is required, but it is beyond the scope of this study.

The positive influence of wide-orbit stellar companions on the appearance of hot Jupiters around M dwarfs is similar to that of Sun-like star counterparts (H. Ngo et al. 2015; C. Fontanive et al. 2019). While the exact reason is still under debate, we discuss two possible pathways to produce such a beneficial effect (see also H. Ngo et al. 2016): promoting planet formation or accelerating the subsequent orbital migration. A higher multiplicity rate might be conducive to hot Jupiter formation by enhancing the formation efficiency via high-density spiral arms induced by stellar companions (K. Wagner et al. 2015; N. K. Reynolds et al. 2021). With more solid materials and high gas density within these spiral arms, massive cores or pebbles are more likely to grow there, triggering the birth of large planets. On the other hand, wide-orbit companions could excite the orbits of "cold" planets and drive inward migration through the Kozai–Lidov effect (D. Fabrycky & S. Tremaine 2007; S. Naoz et al. 2011). The tidal force would then circularize the orbits, leaving behind "hot" planets with short orbital periods. Using Equation (42) in J. M. O. Antognini (2015) and assuming that Jupiter-like planets formed at the snow line $r_{\rm snow} = 2.7(M_*/M_\odot)^{1.75}$ au (S. Ida & D. N. C. Lin 2005), and that comoving stellar companions have circular orbits, we perform a rough estimation of the Kozai–Lidov effect timescales $\tau_{\rm KL}$ of 13 systems that have wide-orbit stellar companions. The masses of stellar companions are estimated through the Gaia G-band magnitude difference with respect to the host star (E. E. Mamajek & L. A. Hillenbrand 2008), except for TOI-5628B that we have the mass determined. We find that $\tau_{\rm KL}$ ranges from about 10^{-3} Gyr to 100 Gyr, with nine systems (69%) having $\tau_{\rm KL}$ smaller than 10 Gyr, indicating that the Kozai–Lidov mechanism is dynamically efficient during the orbital evolution in the majority of these systems. Nevertheless, we note that the assumptions we used above are simplified and might not be realistic, which requires further investigation. In either scenario, our findings, together with results on Sun-like stars, provide a unique constraint that should be reproduced by planet formation simulations. Stellar obliquity studies on both hot and warm Jupiters around M dwarfs (e.g., T. Gan et al. 2024) will offer a valuable test of these competing theories.

5. Conclusions

In this work, we report the discovery and characterization of TOI-5628Ab, a giant planet transiting a mid-M dwarf ($M_* = 0.36 \pm 0.02\,M_\odot$) every 4.34 days, accompanied by a wide-orbit WD with a mass of $0.59 \pm 0.16\,M_\odot$ at a projected separation of about 2500 au. The planet TOI-5628Ab has a radius of $0.74 \pm 0.04\,R_{\rm J}$ and a mass of $0.09 \pm 0.04\,M_{\rm J}$ with a 3σ upper limit of $0.22\,M_{\rm J}$. Building on this system, we conduct a systematic search for comoving stellar companions at projected distances between 100 and 10,000 au around all M dwarfs hosting confirmed giant planets with orbital periods shorter than 10 days and radii greater than $0.7\,R_{\rm J}$. We measure a multiplicity rate of $P(\text{Comp}|\text{HJ}) = 34.2\% \pm 9.5\%$ for the planet sample, which is significantly higher than the value of field M stars with $P(\text{Comp}) = 5.3\% \pm 3.7\%$ by approximately a factor of 6. Our results indicate that a wide-orbit stellar companion between 100 and 10,000 au can facilitate the growth of short-period giant planets around M dwarfs with masses $0.21 \leqslant M_* \leqslant 0.64\,M_\odot$, and high-eccentricity migration may be an important route to produce such systems.

Acknowledgments

T.G. and S.M. acknowledge support by the National Natural Science Foundation of China (No. 12133005). T.G. and E.P. acknowledge financial support from the Agencia Estatal de Investigación of the Ministerio de Ciencia e Innovación MCIN/AEI/10.13039/501100011033 and the ERDF "A way of making Europe" through projects PID2021-125627OB-C32 and PID2024-158486OB-C32, and the funding from the European Union (ERC AdvG SPEAR, GA 101200674). Funding for K.B. was provided by the European Union (ERC AdG SUBSTELLAR, GA 101054354). G.D. acknowledges funding from Magdalen College, Oxford. This work is partly supported by JSPS KAKENHI grant Nos. JP24H00017, JP25K24620, JP26H01402, JP26K00755, and JP24K00689. A.L., É.A., C.C., R.D., and N.J.C. acknowledge the financial support of the Fonds de recherche du Québec - Secteur Nature et technologies (FRQ-NT) through the Centre de recherche en astrophysique du Québec as well as the support from the Trottier Family Foundation and the Trottier Institute for Research on Exoplanets. A.L. acknowledges support from the FRQ-NT under file #349961. É.A. and R.D. acknowledge support from the Canada Foundation for Innovation (CFI) program, the Université de Montréal and Université Laval, the Canada Economic Development (CED) program, and the Ministere of Economy, Innovation and Energy (MEIE). S.M. G. acknowledges the support of the Natural Sciences and Engineering Research Council of Canada (NSERC) and is partially funded through an NSERC Postdoctoral Fellowship (PDF). K.A.C. acknowledges support from the TESS mission via subaward s3449 from MIT and NASA grants 80NSSC24K1889 and 80NSSC26K0081.

This research uses data obtained through the Telescope Access Program (TAP), which has been funded by the TAP association, including Center for Astronomical Mega-Science CAS(CAMS), PKU, THU, USTC, and WLU.

Based on observations obtained at the Canada–France–Hawaii Telescope (CFHT), which is operated from the summit of Maunakea by the National Research Council of Canada, the Institut National des Sciences de l'Univers of the Centre National de la Recherche Scientifique of France, and the University of Hawaii. The observations at the Canada–France–Hawaii Telescope were performed with care and respect from the summit of Maunakea, which is a significant cultural and historic site. Based on observations obtained with SPIRou, an international project led by Institut de Recherche en Astrophysique et Planétologie, Toulouse, France.

Funding for the TESS mission is provided by NASA's Science Mission Directorate. We acknowledge the use of public TESS data from pipelines at the TESS Science Office and at the TESS Science Processing Operations Center. Resources supporting this work were provided by the NASA High-End Computing (HEC) Program through the NASA Advanced Supercomputing (NAS) Division at Ames Research Center for the production of the SPOC data products. This research has made use of the Exoplanet Follow-up Observation Program website, which is operated by the California Institute of Technology, under contract with the National Aeronautics and Space Administration under the Exoplanet Exploration Program. This Letter includes data collected by the *TESS* mission, which are publicly available from the Mikulski Archive for Space Telescopes (MAST). All 2 minute TESS data (TESS Team 2021a) and TPFs (TESS Team 2021b) used in this work can be accessed via MAST.

This work has made use of data from the European Space Agency (ESA) mission Gaia (https://www.cosmos.esa.int/gaia), processed by the Gaia Data Processing and Analysis Consortium (DPAC, https://www.cosmos.esa.int/web/gaia/dpac/consortium). Funding for the DPAC has been provided by national institutions, in particular the institutions participating in the Gaia Multilateral Agreement.

This article is based on observations made with the MuSCAT2 instrument, developed by ABC, at Telescopio Carlos Sánchez operated on the island of Tenerife by the IAC in the Spanish Observatorio del Teide. This work is partly supported by JSPS KAKENHI grant Nos. JP18H01265 and JP18H05439, and JST PRESTO grant No. JPMJPR1775.

This work makes use of observations from the LCOGT network. Part of the LCOGT telescope time was granted by NOIRLab through the Mid-Scale Innovations Program (MSIP), which is funded by NSF.

TRAPPIST is funded by the Belgian Fund for Scientific Research (Fond National de la Recherche Scientifique, FNRS) under the grant FRFC 2.5.594.09.F, with the participation of the Swiss National Science Foundation (SNF). M.G. and E.J. are F.R.S.-FNRS Research Directors.

The ULiege's contribution to SPECULOOS has received funding from the European Research Council under the European Union's Seventh Framework Programme (FP/2007-2013) (grant Agreement No. 336480/SPECULOOS), from the Balzan Prize and Francqui Foundations, from the Belgian Scientific Research Foundation (F.R.S.-FNRS; grant No. T.0109.20), from the University of Liege, and from the ARC grant for Concerted Research Actions financed by the Wallonia-Brussels Federation. The Cambridge contribution is supported by a grant from the Simons Foundation (PI Queloz, grant No. 327127). J.d.W. and M.I.T. gratefully acknowledge financial support from the Heising–Simons Foundation, Dr. and Mrs. Colin Masson and Dr. Peter A. Gilman for Artemis, the first telescope of the SPECULOOS-North network situated in Tenerife, Spain. The Birmingham contribution to SPECULOOS has received fund from the European Research Council (ERC) under the European Union's Horizon 2020 research and innovation program (grant agreement No. 803193/BEBOP), from the MERAC foundation, and from the Science and Technology Facilities Council (STFC; grant Nos. ST/S00193X/1, ST/W002582/1, and ST/Y001710/1) and from the ERC/UKRI Frontier Research Guarantee program (EP/Z000327/1/CandY).

This material is based upon work supported by the National Aeronautics and Space Administration under Agreement No. 80NSSC21K0593 for the program "Alien Earths." The results reported herein benefited from collaborations and/or information exchange within NASA's Nexus for Exoplanet System Science (NExSS) research coordination network sponsored by NASA's Science Mission Directorate. Visiting Astronomer at the Infrared Telescope Facility, which is operated by the University of Hawaii under contract 80HQTR24DA010 with the National Aeronautics and Space Administration.

Facilities: TESS, Gaia, CFHT, IRTF, Shane, Hale, Gemini: Gillett, LCOGT, SPECULOOS-Northern, TRAPPIST, Sanchez.

Software: AstroImageJ (K. A. Collins et al. 2017), astroquery (A. Ginsburg et al. 2019), astropy (Astropy Collaboration et al. 2013, 2018, 2022), juliet (N. Espinoza et al. 2019), batman (L. Kreidberg 2015), radvel (B. J. Fulton et al. 2018).

Appendix A
Ground-based Observations

A.1. Photometric Observations

In this section, we present the details of ground-based photometric observations. All light curves are shown in Figure A1.

A.1.1. LCOGT

We collected three transits of TOI-5628Ab using 1 m telescopes from the Las Cumbres Observatory Global Telescope (LCOGT) network (T. M. Brown et al. 2013) on UT 2022 June 9, UT 2023 January 25, and UT 2023 March 19. We carried out observations in z', r', and g' bands from Teide Observatory, South African Astronomical Observatory (SAAO), and Cerro Tololo Interamerican Observatory (CTIO) with exposure times of 500 s, 500 s, and 600 s, respectively. All three observations were conducted with the Sinistro cameras, with a field of view (FOV) of $26' \times 26'$ and a plate scale of $0\farcs389$ pixel^{-1}. Except for the second observation that was stopped before the egress, the other two runs covered the full transit event. The raw data were calibrated with the BANZAI pipeline (C. McCully et al. 2018), and we then employed the AstroImageJ software (K. A. Collins et al. 2017) to perform the photometric analysis on the reduced images. We confirmed the achromatic transit signal on the target.

A.1.2. SPECULOOS

We used the Search for habitable Planets EClipsing ULtra-cOOl Stars (SPECULOOS; L. Delrez et al. 2018;

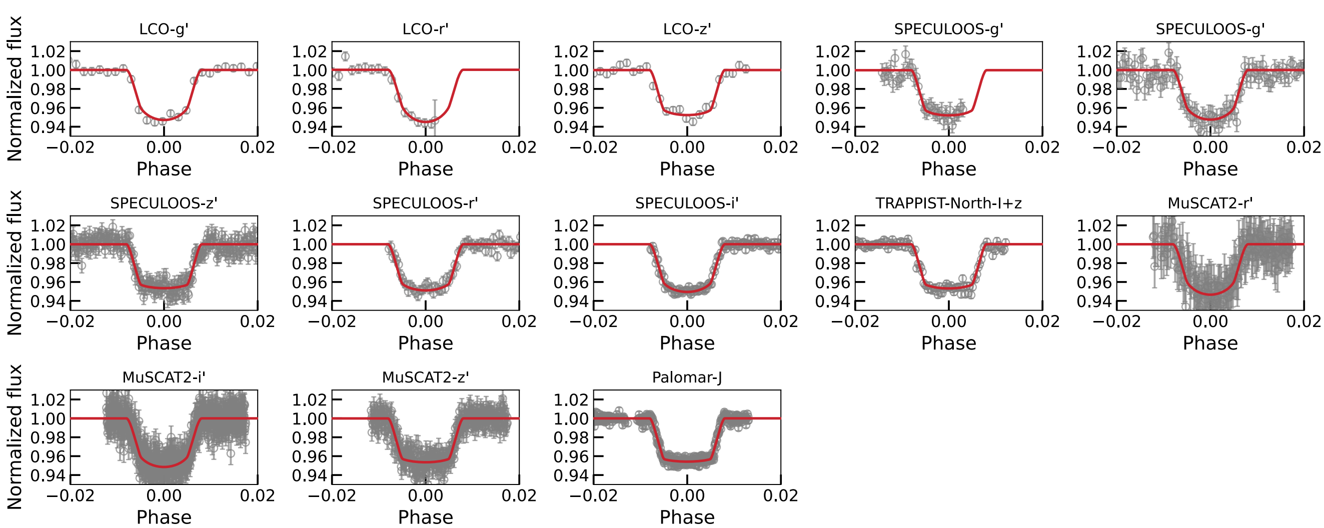

Figure A1. Phase-folded ground-based photometric observations of TOI-5628Ab along with the best-fit transit models shown in red from the joint analysis.

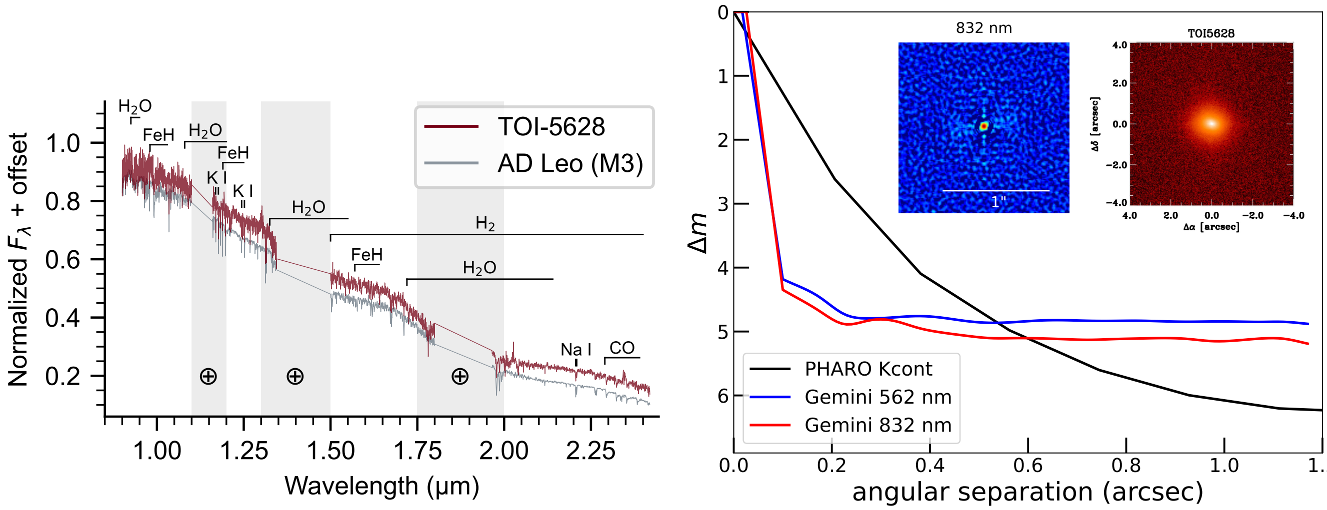

Figure A2. Left panel: SpeX SXD spectrum of TOI-5628A (red) and the comparison spectrum of an M3V dwarf, AD Leo (gray), from the IRTF Spectral Library (J. T. Rayner et al. 2009). Strong atomic and molecular features are marked. Right panel: 5σ contrast curves for TOI-5628A from Palomar/PHARO and Gemini-N/‘Alopeke with images shown as inset figures. The comoving WD companion TOI-5628B at about 23″ is outside the FOV of both instruments, and there are no additional close stellar companions within the detection limits.

D. Sebastian et al. 2021; A. Y. Burdanov et al. 2022) 1.0 m network to observe four full transits and one partial transit of TOI-5628A b. Each telescope was equipped with a 2 K × 2 K Andor iKon-L camera with a pixel scale of 0.″35 and an FOV of 12′ × 12′. Four transits were observed with SPECULOOS–South located in Paranal, Chile, and one transit was observed with SPECULOOS-North at Teide Observatory. The first transit was carried out in the Sloan g' filter on UT 2023 January 25. The second and third transits were carried out on UT 2023 March 31 in the Sloan z' and Sloan g' filters. The fourth and fifth transits were observed on UT 2023 May 31 in the Sloan r' and Sloan i' filters. The data reduction and photometric extraction were performed using the PROSE pipeline (L. J. Garcia et al. 2022). The analysis of the resulting light curves did not reveal any transit depth chromaticity.

A.1.3. TRAPPIST-North

TRAPPIST-North (K. Barkaoui et al. 2019) is a 60 cm Ritchey–Chrétien telescope located at Oukaimeden Observatory, and it is equipped with a thermoelectrically cooled 2 K × 2 K Andor iKon-L BEX2-DD CCD camera with a pixel scale of 0.″6, and an FOV of 20′ × 20′. The TRAPPIST-North telescope observed a full transit of TOI-5628Ab in the $I + z$ filter on UT 2023 March 18 with an exposure time of 100 s. Data processing and photometric extraction were done using the PROSE pipeline (L. J. Garcia et al. 2022). The photometric measurements were extracted using an uncontaminated target aperture of 4.″8.

A.1.4. MuSCAT2

We acquired a full transit of TOI-5628Ab on the night of UT 2024 March 30 using the multicolor imager MuSCAT2 (N. Narita et al. 2019) mounted on the 1.52 m Telescopio Carlos Sánchez at Teide Observatory in Spain. MuSCAT2 has an FOV of 7.′4 × 7.′4 with a pixel scale of 0.″44 pixel^{-1}, and it allows for conducting observations simultaneously in four bands (g, r, i, and z_s). After standard dark and flat calibration, the photometric analysis was performed using the MuSCAT2 pipeline (H. Parviainen et al. 2019), which optimized the aperture to minimize the photometric dispersion and modeled the light curve with instrumental systematic effects included. The exposure times were set to 60 s in g and r, 15 s in i, and 30 s in z_s. We excluded the g-band data due to its low SNR and large scatter.

A.1.5. Wide-field Infrared Camera

We observed one transit of TOI-5628 in the J band on UT 2024 April 17 using the Wide-field InfraRed Camera (WIRC; J. C. Wilson et al. 2003; S. Tinyanont et al. 2019) at the prime focus of the 200 inch Hale Telescope at Palomar Observatory with an exposure time of 20 s. The airmass varied from 1.03 to 1.41 across the observation. The calibration and photometry analysis were performed using exowirc (S. Vissapragada et al. 2020) and photutils (L. Bradley et al. 2016), with an optimized aperture radius that minimized the scatter of the light curve. We cleaned the light curve through a prefit using a median-filtered light curve, followed by σ clipping, resulting in 517 points spanning the transit.

A.2. Spectroscopic Observations

A.2.1. IRTF/SpeX Observation on TOI-5628A

We obtained aν NIR spectrum of TOI-5628A with the SpeX spectrograph (J. T. Rayner et al. 2003) on the 3.2 m NASA Infrared Telescope Facility (IRTF) on UT 2022 July 21. We used the short-wavelength cross-dispersed (SXD) mode with the 0.″3 × 15″ slit aligned to the parallactic angle, yielding spectra spanning 0.82–2.42 μm at a resolving power of $R \sim 2000$. Conditions were clear with seeing of 0.″9. We collected six 300 s exposures at an average airmass of 1.7, nodding along the slit in an ABBA pattern, followed by the standard set of SXD flat-field and arc-lamp calibrations and six 10 s exposures of the A0 V telluric standard at a similar airmass. The data were reduced with Spextool v4.1 (M. C. Cushing et al. 2004), following a standard approach detailed previously (M. Ghachoui et al. 2024; K. Barkaoui et al. 2025). The final spectrum, shown in the left panel of Figure A2, has a median SNR of 79 per resolution element.

A.2.2. Shane/Kast Observation on TOI-5628B

We observed the spectrum of TOI-5628B with the Kast Double Spectrograph on the Shane 3 m telescope at Lick Observatory on the night of UT 2022 June 27. Given the faintness of the star, we adopted exposure times of 3000 s and 1500 s for the blue (3700–5400 Å) and red (5900–9000 Å) bands, respectively. Data were reduced using the `kastredux` package (A. Burgasser 2026). The reduced spectrum is shown in the bottom panel of Figure B1.

A.3. High-angular-resolution Imaging Observations

A.3.1. Palomar/PHARO

We observed TOI-5628A on UT 2024 February 15 with the Palomar High Angular Resolution Observer (PHARO; T. L. Hayward et al. 2001), which is an adaptive optics imaging instrument having a plate scale of $0\farcs025$ pixel^{-1} mounted on the 5 m Hale Telescope. The observation was performed in *the K*cont filter with an estimated point-spread function (PSF) of $0\farcs18$, reaching a contrast of about 4.981 mag at $0\farcs5$. The data were reduced with the pipeline introduced in (E. Furlan et al. 2017). No nearby sources were identified within the detection limits achieved (see Figure A2).

A.3.2. Gemini-N/'Alopeke

TOI-5628A was also observed on UT 2024 May 24 using the 'Alopeke speckle instrument on the Gemini North 8 m telescope (N. J. Scott et al. 2021; S. B. Howell & E. Furlan 2022). 'Alopeke provides simultaneous speckle imaging in two bands (562 nm and 832 nm) with output data products including a reconstructed image with robust contrast limits on companion detections. 12 sets of 1000 × 0.06 s images were obtained and processed in our standard reduction pipeline (S. B. Howell et al. 2011). Figure A2 shows our final contrast curves and the 832 nm reconstructed speckle image. We find that TOI-5628A does not have any companion brighter than 5 mag below that of the target star from the 8 m telescope diffraction limit (20 mas) out to $1\farcs2$. At the distance of TOI-5628A ($d = 110$ pc), these angular limits correspond to spatial limits of 2.2–132 au.

Appendix B
The SEDs of TOI-5628A and TOI-5628B, and the Shane/Kast Spectrum of TOI-5628B

The top panels of Figure B1 present the broadband photometry of TOI-5628A and TOI-5628B along with the best-fit SED models. The bottom panel of Figure B1 shows the Shane/Kast spectrum of TOI-5628B.

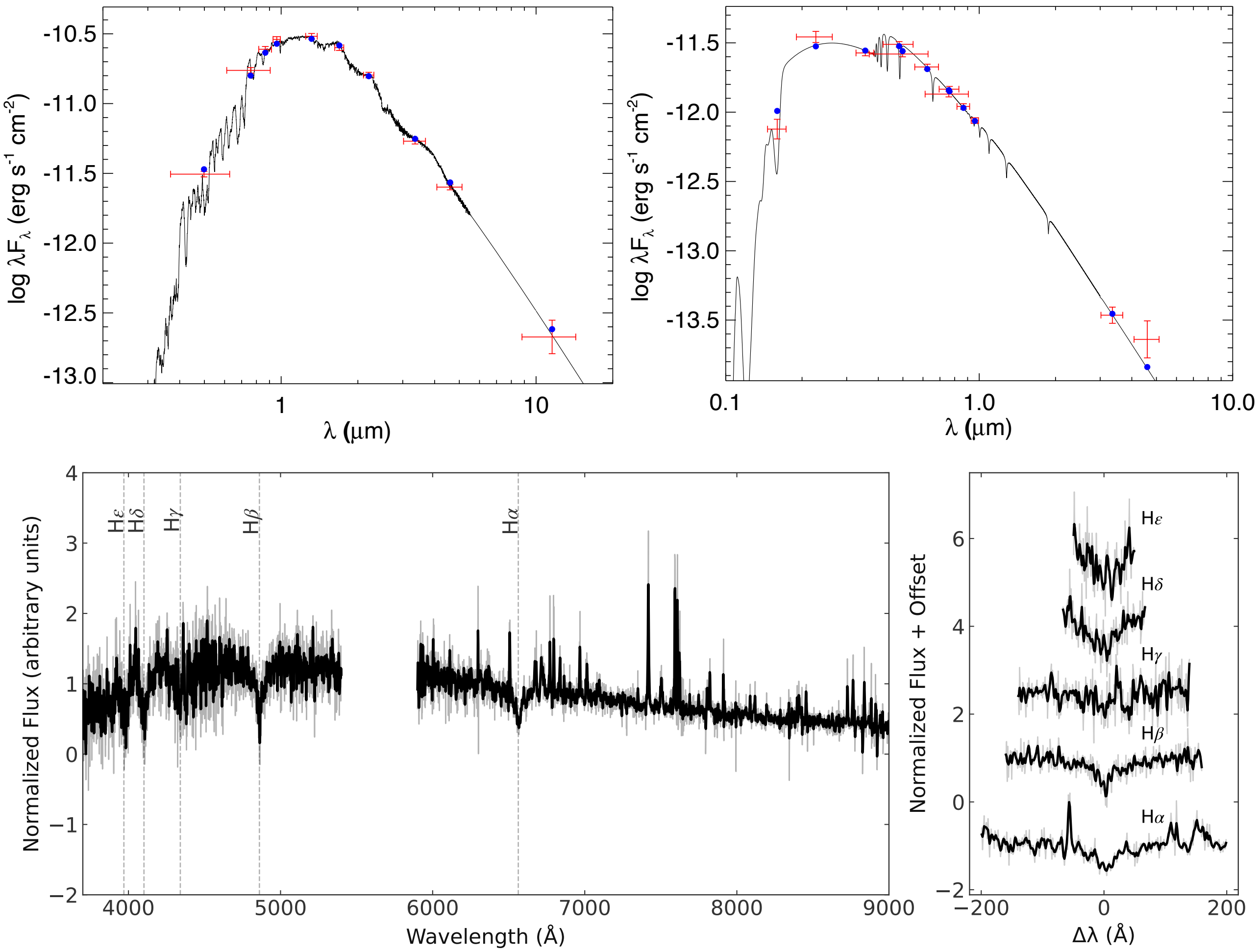

Figure B1. SED of TOI-5628A (Top left) and the associated WD TOI-5628B (Top right). Red symbols represent the observed photometric measurements, where the horizontal bars represent the effective width of the passband. Blue dots are the model fluxes from the best-fit PHOENIX (left) and D. Koester 2010 (right) atmosphere models (black). Bottom left: The stitched blue (3700–5400 Å) and red (5900–9000 Å) Shane/Kast spectrum of TOI-5628B, normalized to an arbitrary continuum level. The raw spectrum is shown in gray, whereas a Gaussian-smoothed spectrum ($\sigma = 1$ Å) is plotted in black. Clear Balmer absorption features are marked with dashed vertical lines. Bottom right: normalized Balmer line profiles plotted as a function of $\Delta\lambda$ from line center. Each line is vertically offset for clarity. These spectral features confirm the DA WD nature of TOI-5628B.

Appendix C
The ZTF Light Curve of TOI-5628A

Figure C1 shows the long-term light curve of TOI-5628A from ZTF, where a 27.9 day photometric modulation can be seen in the data.

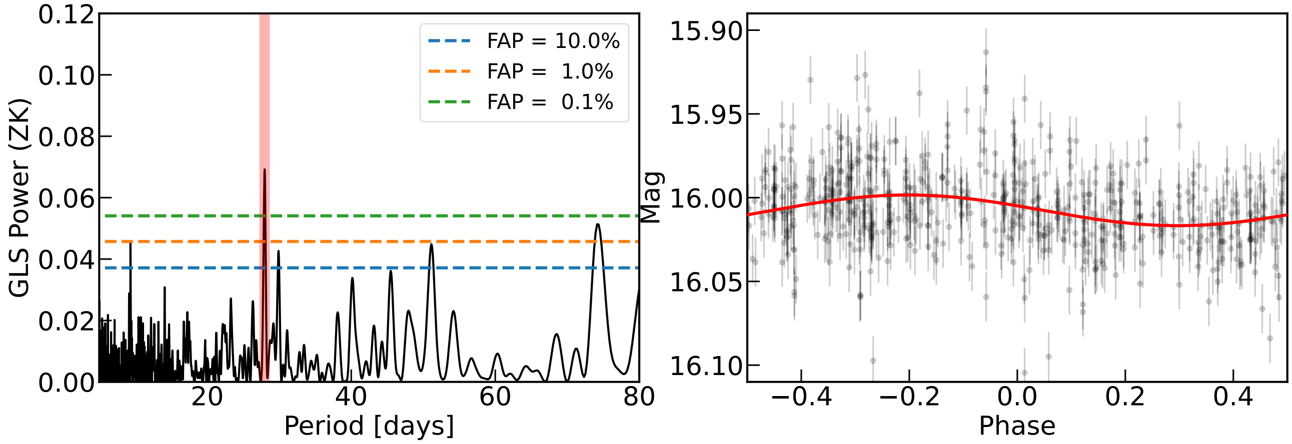

Figure C1. Left panel: GLS periodogram of the ZTF light curve. The vertical red line represents the rotational period inferred for TOI-5628A. The FAP levels of 10%, 1%, and 0.1% are shown as horizontal dashed lines with different colors. Right panel: phase-folded ZTF light curve at 27.9 days with the best-fit sinusoidal model, shown as a red solid curve.

ORCID iDs

Tianjun Gan https://orcid.org/0000-0002-4503-9705
Alexandrine L'Heureux https://orcid.org/0009-0005-6135-6769
Charles Cadieux https://orcid.org/0000-0001-9291-5555
Shude Mao https://orcid.org/0000-0001-8317-2788
Enric Pallé https://orcid.org/0000-0003-0987-1593
Sharon X. Wang https://orcid.org/0000-0002-6937-9034
Keivan G. Stassun https://orcid.org/0000-0002-3481-9052
Steve B. Howell https://orcid.org/0000-0002-2532-2853
Benjamin V. Rackham https://orcid.org/0000-0002-3627-1676
Steffani M. Grondin https://orcid.org/0000-0002-0444-8502
Khalid Barkaoui https://orcid.org/0000-0003-1464-9276
Luc Arnold https://orcid.org/0000-0002-0111-1234
Étienne Artigau https://orcid.org/0000-0003-3506-5667
Artem Burdanov https://orcid.org/0000-0001-9892-2406
Adam J. Burgasser https://orcid.org/0000-0002-6523-9536
Douglas A. Caldwell https://orcid.org/0000-0003-1963-9616
David R. Ciardi https://orcid.org/0000-0002-5741-3047
Karen A. Collins https://orcid.org/0000-0001-6588-9574
Neil J. Cook https://orcid.org/0000-0003-4166-4121
René Doyon https://orcid.org/0000-0001-5485-4675
Georgina Dransfield https://orcid.org/0000-0002-3937-630X
Akihiko Fukui https://orcid.org/0000-0002-4909-5763
Michaël Gillon https://orcid.org/0000-0003-1462-7739
Emmanuel Jehin https://orcid.org/0000-0001-8923-488X
Felipe Murgas https://orcid.org/0000-0001-9087-1245
Norio Narita https://orcid.org/0000-0001-8511-2981
Federico R. Noguer https://orcid.org/0000-0003-4295-7313
Howard M. Relles https://orcid.org/0009-0009-5132-9520
Avi Shporer https://orcid.org/0000-0002-1836-3120
Molly N. Simon https://orcid.org/0000-0001-8536-0942
Abderahmane Soubkiou https://orcid.org/0000-0002-0345-2147
Christopher A. Theissen https://orcid.org/0000-0002-9807-5435
Mathilde Timmermans https://orcid.org/0009-0008-2214-5039
Amaury H. M. J. Triaud https://orcid.org/0000-0002-5510-8751
Robert T. Zellem https://orcid.org/0000-0001-7547-0398
S. Zúñiga-Fernández https://orcid.org/0000-0002-9350-830X
Celso P. Machado https://orcid.org/0000-0003-3320-415X
Ian R. Mason https://orcid.org/0009-0000-4995-8875
Michele T. Mazzucato https://orcid.org/0000-0002-2204-6064
Jingyuan Zhao https://orcid.org/0000-0002-2770-3481

References

Akeson, R. L., Chen, X., Ciardi, D., et al. 2013, PASP, 125, 989
Aller, A., Lillo-Box, J., Jones, D., Miranda, L. F., & Barceló Forteza, S. 2020, A&A, 635, A128
Antognini, J. M. O. 2015, MNRAS, 452, 3610
Artigau, É., Cadieux, C., Cook, N. J., et al. 2022, AJ, 164, 84
Astropy Collaboration, Price-Whelan, A. M., Lim, P. L., et al. 2022, ApJ, 935, 167
Astropy Collaboration, Price-Whelan, A. M., Sipőcz, B. M., et al. 2018, AJ, 156, 123
Astropy Collaboration, Robitaille, T. P., Tollerud, E. J., et al. 2013, A&A, 558, A33
Barkaoui, K., Burdanov, A., Hellier, C., et al. 2019, AJ, 157, 43
Barkaoui, K., Korth, J., Gaidos, E., et al. 2025, A&A, 695, A281
Bellm, E. C., Kulkarni, S. R., Graham, M. J., et al. 2019, PASP, 131, 018002
Benedict, G. F., Henry, T. J., Franz, O. G., et al. 2016, AJ, 152, 141
Bernabò, L. M., Kanodia, S., Cañas, C. I., et al. 2024, AJ, 168, 273
Boyajian, T. S., van Belle, G., & von Braun, K. 2014, AJ, 147, 47
Bradley, L., Sipocz, S., Robitaille, T., et al. 2016, Photutils: Photometry tools, Astrophysics Source Code Library, ascl:1609.011
Brown, T. M., Baliber, N., Bianco, F. B., et al. 2013, PASP, 125, 1031
Bryant, E. M., Bayliss, D., Hartman, J. D., et al. 2024, MNRAS, 533, 3893
Bryant, E. M., Bayliss, D., & Van Eylen, V. 2023, MNRAS, 521, 3663
Burdanov, A. Y., de Wit, J., Gillon, M., et al. 2022, PASP, 134, 105001
Burgasser, A. 2026, aburgasser/kastredux: v1.1.4, Zenodo, doi:10.5281/zenodo.18333308
Burgasser, A. J. & Splat Development Team 2017, ASInC, 14, 7
Burn, R., Schlecker, M., Mordasini, C., et al. 2021, A&A, 656, A72
Cañas, C. I., Kanodia, S., Libby-Roberts, J., et al. 2023, AJ, 166, 30
Catalán, S., Isern, J., García-Berro, E., & Ribas, I. 2008, MNRAS, 387, 1693
Chatterjee, S., Ford, E. B., Matsumura, S., & Rasio, F. A. 2008, ApJ, 686, 580
Christiansen, J. L., McElroy, D. L., Harbut, M., et al. 2025, PSJ, 6, 186
Clark, C. A., van Belle, G. T., Horch, E. P., et al. 2024, AJ, 167, 174
Collins, K. A., Kielkopf, J. F., Stassun, K. G., & Hessman, F. V. 2017, AJ, 153, 77
Cook, N. J., Artigau, É., Doyon, R., et al. 2022, PASP, 134, 114509
Cummings, J. D., Kalirai, J. S., Tremblay, P.-E., Ramirez-Ruiz, E., & Choi, J. 2018, ApJ, 866, 21
Cushing, M. C., Rayner, J. T., & Vacca, W. D. 2005, ApJ, 623, 1115
Cushing, M. C., Vacca, W. D., & Rayner, J. T. 2004, PASP, 116, 362
Cutri, R. M., Skrutskie, M. F., van Dyk, S., et al. 2003, VizieR Online Data Catalog, II/246,
Dawson, R. I., & Johnson, J. A. 2018, ARA&A, 56, 175
Delrez, L., Gillon, M., & Queloz, D. 2018, SPIE, 10700, 107001I
Donati, J. F., Kouach, D., Moutou, C., et al. 2020, MNRAS, 498, 5684
Dransfield, G., Timmermans, M., Sebastian, D., et al. 2026, MNRAS, 547, stag448
Eggleton, P. P., Kiseleva, L. G., & Hut, P. 1998, ApJ, 499, 853
Eisner, N. L., Barragán, O., & Lintott, C. 2021, MNRAS, 501, 4669
El-Badry, K., Rix, H.-W., & Heintz, T. M. 2021, MNRAS, 506, 2269
El-Badry, K., Rix, H.-W., Tian, H., Duchêne, G., & Moe, M. 2019, MNRAS, 489, 5822
Espinoza, N. 2018, RNAAS, 2, 209
Espinoza, N., Kossakowski, D., & Brahm, R. 2019, MNRAS, 490, 2262
Fabrycky, D., & Tremaine, S. 2007, ApJ, 669, 1298
Fontanive, C., Rice, K., Bonavita, M., et al. 2019, MNRAS, 485, 4967
Ford, E. B., & Rasio, F. A. 2008, ApJ, 686, 621
Foreman-Mackey, D., Agol, E., Ambikasaran, S., & Angus, R. 2017, AJ, 154, 220
Frensch, Y. G. C., Bouchy, F., Lo Curto, G., et al. 2026, A&A, 707, A73
Fulton, B. J., Petigura, E. A., Blunt, S., & Sinukoff, E. 2018, PASP, 130, 044504
Furlan, E., Ciardi, D. R., Everett, M. E., et al. 2017, AJ, 153, 71
Gaia Collaboration, Brown, A. G. A., Vallenari, A., et al. 2018, A&A, 616, A1
Gaia Collaboration, Vallenari, A., Brown, A. G. A., et al. 2023, A&A, 674, A1
Gan, T., Cadieux, C., Jahandar, F., et al. 2023a, AJ, 166, 165
Gan, T., Lin, Z., Wang, S. X., et al. 2022, MNRAS, 511, 83
Gan, T., Theissen, C. A., Wang, S. X., Burgasser, A. J., & Mao, S. 2025, ApJS, 276, 47
Gan, T., Wang, S. X., Dai, F., et al. 2024, ApJL, 969, L24
Gan, T., Wang, S. X., Wang, S., et al. 2023b, AJ, 165, 17
Garcia, L. J., Timmermans, M., Pozuelos, F. J., et al. 2022, MNRAS, 509, 4817
Ghachoui, M., Rackham, B. V., Dévora-Pajares, M., et al. 2024, A&A, 690, A263
Ginsburg, A., Sipőcz, B. M., Brasseur, C. E., et al. 2019, AJ, 157, 98
Glusman, R. I., Cañas, C. I., Kanodia, S., et al. 2026, AJ, 171, 146
Hartman, J. D., Bayliss, D., Brahm, R., et al. 2024, AJ, 168, 202
Hayward, T. L., Brandl, B., Pirger, B., et al. 2001, PASP, 113, 105
Henden, A. A., Templeton, M., Terrell, D., et al. 2016, yCat, II/336
Howell, S. B., Everett, M. E., Sherry, W., Horch, E., & Ciardi, D. R. 2011, AJ, 142, 19
Howell, S. B., & Furlan, E. 2022, FrASS, 9, 871163
Husser, T. O., Wende-von Berg, S., Dreizler, S., et al. 2013, A&A, 553, A6

Hut, P. 1981, A&A, 99, 126
Hwang, H.-C., Ting, Y.-S., Schlaufman, K. C., Zakamska, N. L., & Wyse, R. F. G. 2021, MNRAS, 501, 4329
Ida, S., & Lin, D. N. C. 2005, ApJ, 626, 1045
Jackson, B., Greenberg, R., & Barnes, R. 2008, ApJ, 678, 1396
Jenkins, J. M., Twicken, J. D., McCauliff, S., et al. 2016, SPIE, 9913, 99133E
Jordán, A., Hartman, J. D., Bayliss, D., et al. 2022, AJ, 163, 125
Kanodia, S., Gupta, A. F., Cañas, C. I., et al. 2024, AJ, 168, 235
Kennedy, G. M., & Kenyon, S. J. 2008, ApJ, 673, 502
Kipping, D. M. 2013, MNRAS, 435, 2152
Koester, D. 2010, MmSAI, 81, 921
Kozai, Y. 1962, AJ, 67, 591
Kreidberg, L. 2015, PASP, 127, 1161
Lasker, B. M., Doggett, J., McLean, B., et al. 1996, ASPC, 101, 88
Laughlin, G., Bodenheimer, P., & Adams, F. C. 2004, ApJL, 612, L73
Lépine, S., Hilton, E. J., Mann, A. W., et al. 2013, AJ, 145, 102
Lidov, M. L. 1962, P&SS, 9, 719
Liu, B., & Ji, J. 2020, RAA, 20, 164
Luyten, W. J. 1963, Bruce proper motion survey. The general catalogue, 1, 2
Mamajek, E. E., & Hillenbrand, L. A. 2008, ApJ, 687, 1264
Mann, A. W., Brewer, J. M., Gaidos, E., Lépine, S., & Hilton, E. J. 2013, AJ, 145, 52
Mann, A. W., Feiden, G. A., Gaidos, E., Boyajian, T., & von Braun, K. 2015, ApJ, 804, 64
Mann, A. W., Dupuy, T., Kraus, A. L., et al. 2019, ApJ, 871, 63
Masci, F. J., Laher, R. R., Rusholme, B., et al. 2019, PASP, 131, 018003
Matson, R. A., Gore, R., Howell, S. B., et al. 2025, AJ, 169, 76
McCully, C., Volgenau, N. H., Harbeck, D.-R., et al. 2018, SPIE, 10707, 107070K
Moe, M., & Kratter, K. M. 2021, MNRAS, 507, 3593
Moe, M., Kratter, K. M., & Badenes, C. 2019, ApJ, 875, 61
Muirhead, P. S., Dressing, C. D., Mann, A. W., et al. 2018, AJ, 155, 180
Naoz, S. 2016, ARA&A, 54, 441
Naoz, S., Farr, W. M., Lithwick, Y., Rasio, F. A., & Teyssandier, J. 2011, Natur, 473, 187
Narita, N., Fukui, A., Kusakabe, N., et al. 2019, JATIS, 5, 015001
Ngo, H., Knutson, H. A., Hinkley, S., et al. 2015, ApJ, 800, 138
Ngo, H., Knutson, H. A., Hinkley, S., et al. 2016, ApJ, 827, 8
Offner, S. S. R., Moe, M., Kratter, K. M., et al. 2023, ASPC, 534, 275
Osborn, A., Cloutier, R., Bourrier, V., et al. 2026, A&A, 709, A23
Parc, L., Bouchy, F., Cook, N. J., et al. 2025, A&A, 702, A138
Parviainen, H., Tingley, B., Deeg, H. J., et al. 2019, A&A, 630, A89
Pecaut, M. J., & Mamajek, E. E. 2013, ApJS, 208, 9
Petrovich, C. 2015, ApJ, 805, 75
Raddi, R., Torres, S., Rebassa-Mansergas, A., et al. 2022, A&A, 658, A22
Raghavan, D., McAlister, H. A., Henry, T. J., et al. 2010, ApJS, 190, 1
Rasio, F. A., & Ford, E. B. 1996, Sci, 274, 954
Rayner, J. T., Cushing, M. C., & Vacca, W. D. 2009, ApJS, 185, 289
Rayner, J. T., Toomey, D. W., Onaka, P. M., et al. 2003, PASP, 115, 362
Reji, V., Kanodia, S., Ninan, J. P., et al. 2025, AJ, 169, 187
Reynolds, N. K., Tobin, J. J., Sheehan, P., et al. 2021, ApJL, 907, L10
Rice, M., Wang, S., Wang, X.-Y., et al. 2022, AJ, 164, 104
Ricker, G. R., Winn, J. N., Vanderspek, R., et al. 2015, JATIS, 1, 014003
Schlegel, D. J., Finkbeiner, D. P., & Davis, M. 1998, ApJ, 500, 525
Scott, N. J., Howell, S. B., Gnilka, C. L., et al. 2021, FrASS, 8, 138
Sebastian, D., Gillon, M., Ducrot, E., et al. 2021, A&A, 645, A100
Smith, J. C., Stumpe, M. C., Van Cleve, J. E., et al. 2012, PASP, 124, 1000
Speagle, J. S. 2020, MNRAS, 493, 3132
Srivastava, A., Doyon, R., Bouchy, F., et al. 2026, A&A, 709, A73
Stassun, K. G., Collins, K. A., & Gaudi, B. S. 2017, AJ, 153, 136
Stassun, K. G., & Torres, G. 2016, AJ, 152, 180
Stassun, K. G., & Torres, G. 2018, ApJ, 862, 61
Stassun, K. G., & Torres, G. 2021, ApJL, 907, L33
Stassun, K. G., Oelkers, R. J., Paegert, M., et al. 2019, AJ, 158, 138
Stumpe, M. C., Smith, J. C., Catanzarite, J. H., et al. 2014, PASP, 126, 100
Stumpe, M. C., Smith, J. C., Van Cleve, J. E., et al. 2012, PASP, 124, 985
TESS Team 2021a, TESS Target Pixel Files - All Sectors, STScI/MAST, doi:10.17909/T9-YK4W-ZC73
TESS Team 2021b, TESS Light Curves—All Sectors, STScI/MAST, doi:10.17909/T9-NMC8-F686
Tinyanont, S., Millar-Blanchaer, M. A., Nilsson, R., et al. 2019, PASP, 131, 025001
Tremblay, P.-E., Bergeron, P., & Gianninas, A. 2011, ApJ, 730, 128
Vincent, O., Barstow, M. A., Jordan, S., et al. 2024, A&A, 682, A5
Vissapragada, S., Jontof-Hutter, D., Shporer, A., et al. 2020, AJ, 159, 108
Wagner, K., Apai, D., Kasper, M., & Robberto, M. 2015, ApJL, 813, L2
Ward-Duong, K., Patience, J., De Rosa, R. J., et al. 2015, MNRAS, 449, 2618
Wilson, J. C., Eikenberry, S. S., Henderson, C. P., et al. 2003, SPIE, 4841, 451
Winters, J. G., Henry, T. J., Jao, W.-C., et al. 2019, AJ, 157, 216
Wright, E. L., Eisenhardt, P. R. M., Mainzer, A. K., et al. 2010, AJ, 140, 1868
Wu, Y., & Lithwick, Y. 2011, ApJ, 735, 109
Zechmeister, M., & Kürster, M. 2009, A&A, 496, 577
Ziegler, C., Tokovinin, A., Briceño, C., et al. 2020, AJ, 159, 19